ZnO-functionalized fly-ash based zeolite for ciprofloxacin antibiotic degradation and pathogen inactivation

Georgiana Amariei, Laura Valenzuela, Ana Iglesias-Juez, Roberto Rosal, MariaVisa. ZnO-functionalized fly-ash based zeolite for ciprofloxacin antibiotic degradation and pathogen inactivation, Journal of Environmental Chemical Engineering, 107603, 2022.

https://doi.org/10.1016/j.seppur.2021.120351

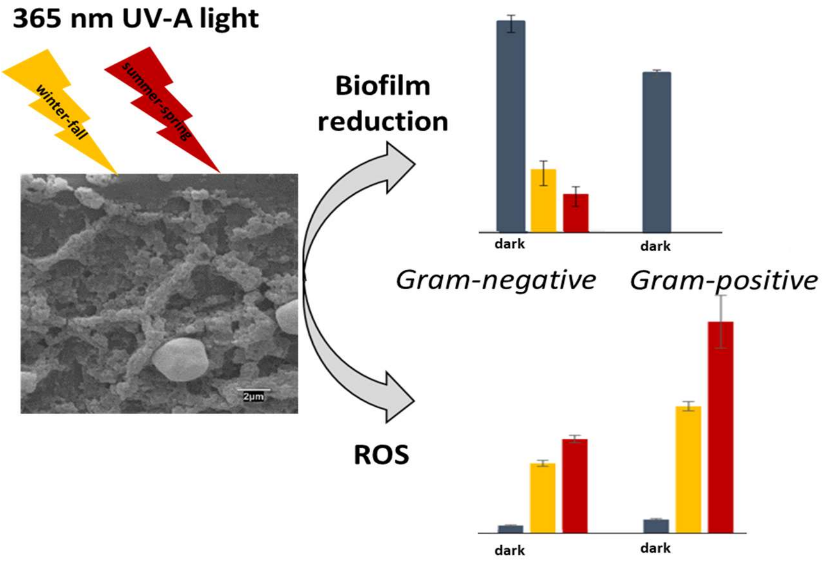

https://www.sciencedirect.com/science/article/abs/pii/S2213343722004766

ZnO-functionalized fly-ash based zeolite for ciprofloxacin antibiotic degradation and pathogen inactivation

Georgiana Amariei[1,2,*], Laura Valenzuela[2], Ana Iglesias-Juez[3], Roberto Rosal, MariaVisa[4]

[1] Department of Biological and Chemical Engineering- Plastic and Polymer Engineering Group, Aarhus University, Aabogade 40, DK-8200, Aarhus N., Denmark

[2] Department of Chemical Engineering, Universidad de Alcalá, 28805 Alcalá de Henares, Madrid, Spain

[3] Instituto de Catálisis y Petroleoquímica, ICP-CSIC, Marie Curie 2, 28049 Madrid, Spain

[4] Research Center: Renewable Energy Systems and Recycling, Transilvania University of Brasov, Eroilor 29, 500036, Brasov, Romania

* Corresponding author: georgiana.amariei@bce.au.dk

Abstract

There is an increasing need for photocatalytic materials capable to remove pollutants and to deactivate microorganisms for a wide range of applications. Here we report the preparation of fly ash-based zeolite material in which ZnO was incorporating using an alkaline hydrothermal method. The zeolitic materials were used to functionalized glass substrates through spin-coating technique and characterized by X-ray diffraction, emission spectroscopy, electrophoretic light scattering, and UV–Vis diffuse reflectance, among other techniques. The surface characteristics of the coatings were determined by scanning electron microscopy and water contact angle. The photocatalytic activity of ZnO-functionalized fly-ash based zeolite was assessed by tracking the degradation of the antibiotic ciprofloxacin (CIP) and its antimicrobial capacity by means of the inactivation of the bacteria *Staphylococcus aureus* and *Escherichia coli* under UVA (365 nm) irradiation. The results showed the formation of a sodalite zeolite structure with a band gap of 3.2 eV and photoinduced hydrophilicity. The ZnO-modified fly ash material was able to completely photodegrade CIP in less than 20 min irradiation with 365 nm UVA light, while its non-modified precursor, even displaying a high adsorption capacity was unable to remove the antibiotic after 120 min. The ZnO-zeolitic materials and coatings were able to inactivate bacteria with reductions in the number of viable colonies > 99.9 for *S. aureus* and > 99.0% for *E. coli* after 60 min of irradiation, even on specimens previously allowed to grow a mature biofilm. The zeolitic material also proved a low cytotoxicity to human fibroblast cultures.

Keywords: Fly-ash; Zinc oxide; Zeolite photocatalytic coating; Disinfection; Antibiotic degradation

1. Introduction

The production of energy by combustion gives rise to large amount of fly ashes, a drawback shared by old coal-burning power plants, municipal solid waste incineration plants, and those producing green electricity from biomass [1]. Fly ashes find use in concrete production and other construction practices, and as soil amendment because of its capacity to improve soil physicochemical properties [2]. However, the content of heavy metals is usually too high to allow their use in the aforementioned applications and most of them have been traditionally sent to landfills. The interest of the energy generation industry in developing implementations for fly ashes is mainly driven by the rising costs of developing new disposal sites. Therefore, fly ashes constitute an abundant raw material susceptible to new potential uses, at the same time helping to solve an environmental and economic problem [3]. Depending on their source the composition of fly ash changes, but overall, it is mainly composed of silica, alumina, and calcium and iron oxides with rather homogeneous distributions among particles. Besides, fly ashes contain a number of other elements at trace levels with uneven distribution, which include a wide variety of metals and metalloids together with unburnt carbon and certain organic compounds [4]. Because of the presence of heavy metals and toxic compounds, the improper disposal of fly ashes may cause water and soil pollution with potential environmental and health hazards.

Fly ashes display surface adsorption properties, which granted their use to remove different water contaminants [5]. The composition of fly ashes together with relatively large particle sizes, which favour their recovery, makes them attractive for the production of photocatalytic material. Specifically, fly ashes have been explored as substrate for the immobilization of different photocatalysts, which benefit from the synergistic effect of adsorption and photocatalysis [6]. The incorporation of TiO_2 and other photocatalytic phases to fly ashes has been used to produce a number of photocatalytic materials. AgCl-TiO_2 and $BiVO_4$ have been supported on floating fly ash cenospheres and successfully used for the degradation of aqueous pollutants [7, 8]. ZnO nanofibres were incorporated into fly ashes using electrospinning to create a semiconductor composite photocatalyst, which favoured from the enhanced dispersion of fly ashes onto

https://doi.org/10.1016/j.jece.2022.107603

the surface of the ZnO nanofibers [9]. It has been also shown that certain modifications of fly ashes lead to improvements in composite photocatalytic materials. The activation of fly ash using alkaline treatments enhances the performance of fly ash-TiO_2 photocatalysts when used to remove organic pollutants [10, 11]. The background is that fly ashes can be used to prepare synthetic zeolites of different types, which showed advantages over commercially available zeolitic materials [12].

The development of photoactive materials capable to the simultaneous removal of pollutants and the inactivation of microorganisms is the subject topic of intense research. Photocatalytic phases can act as antimicrobial substances in two ways. Physically, because of the photoinduced hydrophilicity of several semiconductors that results from the formation of photogenerated surface hydroxyl groups in the presence of water [13, 14]. Besides, heterogeneous photocatalysts give rise to a variety of reactive oxygen species (ROS) with strong oxidizing power. Photocatalytic disinfection benefits from the antimicrobial effect of ROS and, although extensively studied in slurry systems, finds its most rational application in the design of self-disinfecting surfaces [15].

Photocatalytic disinfection offers important advantages such as the limited formation of disinfection by-products, and the possible use of solar radiation. In the case of photocatalytic active surfaces, there is also the advantage of avoiding the recovery of powdered materials when used in suspensions. Composites based on fly ashes have shown to display antimicrobial effect. Yan et al. (2018) prepared N-doped TiO_2-fly ash cenospheres and demonstrated their high disinfection efficiency against *Escherichia coli* upon irradiation UVA and 420 nm visible light [16]. With a similar rationale, a geopolymer paste from high calcium fly ash containing nano-titanium dioxide was prepared to create a surface resistant to algae and fungi colonization with good results for loadings of nano-titanium dioxide content up to 5 wt% displayed resistance to algae and fungi with limited impairment of mechanical properties [17].

In this work, we prepared a zeolitic material containing ZnO from raw fly ash from a combusting facility by means of a simple alkaline hydrothermal synthesis. The ZnO-functionalized material was used to prepare active surfaces by spin-coating. The physicochemical properties of the novel zeolitic material, and the surfaces produced with it were investigated using different characterization techniques. The photocatalytic capacity was examined by studying the photocatalytic degradation of the antibiotic ciprofloxacin and the inactivation of the pathogenic strains S. aureus and *E. coli* bacteria under 365 nm irradiation that mimics the solar UVA component.

2. Materials and methods

2.1. Preparation and characterization of the photocatalytic material

Raw fly ash (FA) was obtained from the electro-filter of a combined heat and power plant located in Brasov, Romania. The composition of raw FA is provided in Table 1. The ZnO-FA based zeolite was obtained by hydrothermal treatment under alkaline conditions [18] using $ZnCl_2$ as a modifier and NaOH solution as solvent. Briefly, a mixture of pre-washed FA (55.0 g), NaOH (66.0 g), and $ZnCl_2$ (60 g) was heated for 3 h at 550 °C. After calcination and cooling, the collected material was grounded, resuspended in 800 mL ultrapure water (UW, conductivity > 18 $M\Omega\ cm^{-1}$) and kept for 24 h under constant stirring, at 25 °C. Next, a NaOH solution (80.0 g NaOH in 500 mL UW) was incorporated to the suspension. The slurry was transferred into a stainless autoclave, hydrothermally heated to 100 °C at 5 bar of pressure and stirred at 200 rpm for 72 h. After annealing and cooling, the resultant solid product was recovered by filtration (0.45 µm filter) followed with repeated washing using UW and dried at 50 °C overnight. The obtained ZnO-FA was used as photocatalyst as powder and for coatings.

The elemental composition of FA and ZnO-functionalized zeolitic materials (ZnO-ZFA) was established by Inductively Coupled Plasma Atomic Emission Spectroscopy (ICP-AES, PlasmaQuant® PQ 9000, Analytik Jena) and verified by Energy Dispersive X-ray Spectroscopy (EDX, Hitachi TM-1000). The isoelectric point was determined by zeta potential (ζ-potential) measurement in the region of pH 4.4-9.3 at 25 °C in a Zetasizer Nano ZS (Malvern). The crystal structure of the powders was studied by X-ray Diffraction (XRD, PANalytical X'Pert Pro). UV-vis Diffuse Reflectance Spectra (DRS, Agilent Cary 5000) of the samples were registered and further band-gap was determined. Brunauer-Emmett-Teller (BET) surface area was determined with a Micromeritics Asap 2020 analyser. Prior to each gas sorption experiment, the samples were degassed down at 150 ºC for at 8 h.

To assess the capacity of the material for the separation of the photogenerated electron-hole pairs, transient photocurrent (TPC) measurements were conducted under 365 nm UVA LED light irradiation in a three-electrode cell setup (20 mL of working volume), using graphite paper and Ag/AgCl as counter and reference electrodes, respectively. The working electrodes were prepared by depositing 0.1 mL of a 10 g L^{-1} suspension of the catalysts in ethanol onto sanded and prewashed graphite paper (GP) substrates (SIGRACELL® PV15, SGL Carbon). TPC was performed at +1.0 V vs. Ag/AgCl in 0.1 M Na_2SO_4 with 25 s light on and 25 s off cycles using a Metrohm Autolab PGSTAT101 station.

2.2. Fabrication and characterization of photocatalytic surfaces

For the preparation of the photocatalytic surface, 10 g L^{-1} of ZnO-ZFA in acidic isopropanol (0.5 % v/v nitric acid) was ultrasonically dispersed and stirred overnight. The resultant suspension was deposited on glass support (1 cm x 1 cm) using an WS-650-23B, Laurell Technologies spin-coater. Prior to the coating, the glass substrates were preconditioned by ultrasonic cleaning with detergent, UW, acetone, ethanol, and UW and drying 10 minutes at 150 °C. The spin-coating was performed employing a 0.2 s dynamic dispense at 500 rpm continued by 15 seconds of increasing speed and drying at 1500 and 3500 rpm, respectively. Five cycles of spin-coating were applied, reaching a mass surface density of 0.16 ± 0.07 mg cm^{-2}. After each spin-coating cycle, the specimens were dried 10 minutes at 150 °C to remove the possible residual solvent.

The morphology of coatings was investigated by Scanning Electron Microscopy (SEM, Zeiss DSM 950) at 25 kV. The wettability and hydrophobicity of the spin-coated surfaces was determined by measuring water contact angle (WCA, DSA25, Krüss). The stability and possible leakage of ions from the functionalized surfaces was tested by submerging coated substrates in 2.5 mL cm^{-2} UW (pH 7.2), at 37 °C, for 20 h and the amount of ions was quantified by Total reflection X-Ray Fluorescence (TXRF S2 PicoFox, Bruker) [19].

2.3. Photocatalytic activity

The photocatalytic capacity of ZnO-ZFA was assessed by following the degradation of the antibiotic ciprofloxacin (> 98 % purity, Merck, CIP) and the inactivation of two bacterial strains, the Gram-positive *S. aureus* (CECT 240/ATCC 6538P) and the Gram-negative *E. coli* (CECT 516/ATCC 8739). The photocatalytic assays were performed by means of 365 nm UVA LED (Mightex LED BLS 13000-1) with an irradiance of 180 W m^{-2}.

The photodegradation experiments were carried out with suspensions of 400 mg L-1 FA, 100 mg L^{-1} ZnO (14 nm, PlasmaChem GmbH, Germany) or 500 mg L^{-1} ZnO-ZFA (corresponding to the same amount of fly ash after excluding the weight of ZnO incorporated to the modified FA) and 25 mL of 10 mg L^{-1} CIP solution (pH 4). In addition, solutions of 10 mg L^{-1} CIP without catalyst were used as negative controls for photolysis. The suspensions were kept in the dark for 30 min at 25 °C and magnetically stirred at 100 rpm in contact with CIP solutions. Subsequently, the suspensions were exposed to UVA irradiation with power input per unit volume of 5.1 W L-1. Aliquots of 1.0 mL were extracted at prescribed time (0, 5, 10, 20, 40, 60, 90, and 120 min) and filtered with a 0.2 µm nylon syringe filters. CIP was analysed with Shimadzu UV-2700i UV-vis spectrophotometer, in the 200–800 nm interval. The CIP concentration variation was quantified at the specific absorption wavelength of 277 nm using a calibration curve between 0.5-10 mg L^{-1} [20].

The photo-disinfection capacity of the tested materials was established by determining the decrease in the number of viable colonies (colony forming units, CFU) of the bacteria [21]. The microorganisms were first cultured overnight at 37 °C in nutrient broth (NB, the aqueous solution of 10 g L^{-1} peptone, 5 g L^{-1} beef extract, 5 g L^{-1} sodium chloride, pH 7.0 ± 0.2), under continuous shaking. The bacterial inoculum in the bioassays was adjusted to an initial CFU value of 10^6 cells mL^{-1} using NB 1:500. Two types of experiments were performed, which used powder photocatalyst suspension and a surface functionalize with photocatalytic coating respectively.

The bacterial inactivation experiments with powdered materials in suspension were conducted both in photocatalytic and dark conditions using 16 mg FA, 4 mg ZnO or 20 mg of ZnO-ZFA (corresponding to the same amount of fly ash after excluding the weight of ZnO incorporated to the modified FA). The amount of ZnO-ZFA was calculated for better intercomparison excluding the weight of ZnO as determined from the data shown in Table 1, were incubated with 25 mL of *S. aureus* and *E. coli* inoculum, under continuous stirring (50 rpm) for 60 min. During the runs, aliquots of 500 µL were collected at specific time (0, 5, 10, 20, 40, and 60 min) from the mixtures and the number of viable bacteria was quantified.

Colonization tests on coated surfaces were performed by incubating coated and uncoated glass surfaces (1 cm^2) with 2 mL of bacterial suspension in sterile 24-well plates. Bacterial colonization and biofilm formation was allowed to proceed for 20 h of contact at 37 °C in static and darkness conditions, following the standard guidelines ISO 22196:2011 [21]. Subsequently, the samples were irradiated for 30 and 60 min, which represented 1.0 and 2.0 kW-h m^{-2}, respectively. The UV dose was calculated using NASA Surface Meteorology and Solar Energy Database as a conservative estimation of one third of the average daily incident insolation at the latitude of Madrid. The two irradiances are described in what follows as winter-fall or L(+), and summer-spring or L(++) (19). After irradiation, the CFU both in the liquid fraction and detached from the surfaces was determined. Standard, soya casein digest lecithin polysorbate broth (SCDLP) was used to detach bacteria. Dark control groups were included denoted insofar as L(-).

The number of viable cells was estimated by plate count method following the ISO 22196:2011 [21]. In brief, 10 µL droplets of 10-fold serial dilutions were placed on Petri dishes containing standard methods agar (2.5 g L^{-1} yeast extract, 5 g L^{-1} tryptone, 1 g L^{-1} glucose, 5 g L^{-1} agar powder). The agar plates were maintained at 37 °C overnight. Two replicates with minimum two serial dilutions were included in the CFU calculations.

The generation of ROS was investigated with 2′,7′ dichlorodihydrofluorescein diacetate (H_2DCFDA, Sigma-Aldrich) probe. In brief, H_2DCFDA enter into the bacterial cells and is hydrolysed to dichlorodihydrofluorescein carboxylate anion, which in the presence of ROS is oxidized to the fluorescent DCF [22, 23]. For it, 150 µL of bacterial aliquots were collected during disinfection runs as indicated before and subsequently reacted with 50 µL of a 10 mM H_2DCFDA solution in a black microplate. The fluorescence measurements were conducted with Fluoroskan Ascent FL microplate reader (Thermo Scientific) at $\lambda_{ex/em}$ =485/528 nm, 25 °C, during 30 min. The bacterial membrane cell damage was investigated with fluorescein diacetate (FDA, Sigma-Aldrich) fluorescent staining method [24, 25]. In brief, 195 µL bacterial sample aliquots were incubated with 5 µL dye (0.02 % w/w in DMSO) in 96-black well microplate in a fluorescence reader (Fluoroskan Ascent FL, Thermo Fisher Scientific), at 25 °C. Fluorescence signal was recorded at λex/em of 485-528 nm every 5 min during 30 min.

Reusability of the ZnO-ZFA was explored by incubating coated glass surfaces with 2 mL of bacterial suspension for 20h followed by 30 and 60 min UVA irradiation, as previously described, for four successive cycles. The bacterial inhibition was quantified based on optical density measurements by using crystal violet dye [26]. For this, 200 µL of 0.1% crystal violet solution were added over the surface of samples and incubated for 15 min in order to allow the staining of adhered cells. Then, the samples were rinsed with distilled water to remove the excess stain, air dried, and incubated overnight with 1 mL of 95% ethanol in order to extract crystal violet from cells. Finally, the dye was measured at 590 nm. Prior to each cycle, the samples were washed with PBS and well rinsed distilled water. The effect of organic fouling on disinfection performance of ZnO-ZFA was investigated. ZnO-ZFA coated glass surfaces were incubated with 2 mL of 1 g L^{-1} bovine serum albumin (BSA, Sigma-Aldrich) solution (PBS, 0.1 M, pH 7.2), overnight [27]. Disinfection efficiency of the organic fouled ZnO-ZFA specimens was quantified with crystal violet dye after incubating them with 2 mL of bacterial suspension for 20 h, followed by 30 and 60 min UVA irradiation, as previously described for clean ZnO-ZFA coated glass samples.

2.4. Biocompatibility

The cytotoxic response of ZnO-ZFA was examined with human dermal fibroblasts (hDF, ATCC) following the standard colorimetric MTT assay. An in vitro test was conducted with three amounts of ZnO-ZFA namely 10, 100, and 1000 mg L^{-1}. 24-well sterile plate was inoculated with suspensions of 3×10^5 cells per well and then ZnO-ZFA was added (n = 6). Wells without ZnO-ZFA was used as control (n = 6). The plate was maintained at 37 °C, in a humidified carbon dioxide (5-6.5 %) atmosphere, for 24 h. To quantify the number of viable cells, MTT reagent was reacted with the cells for 4 h and the resultant product was analysed at 570 nm (BioTek Elisa microplates Reader), after prior solubilization in dimethyl sulfoxide. Cell viability was reported as inhibition percentage compared to control.

2.5. Statistical analysis

A two-way analysis of variance (ANOVA) and Tukey's test ($p < 0.05$) were conducted with Statgraphics Centurion XVII software.

3. Results and discussion

3.1. Characterization of zeolite powder and coatings

3.1.1. Characterization of FA and ZnO-ZFA

The elemental composition of FA and ZnO-ZFA as determined by ICP-AES is shown in Table 1. According to the ASTM standards (C618-05) [28], the raw FA used in this work is of F type (pozzolanic) because the sum of the major oxides SiO_2, Al_2O_3 and Fe_2O_3 is > 70 % and CaO < 6.5 %. Besides, the SiO_2:Al_2O_3 ratio (2.41) is compatible with a zeolitic structure [18]. The loading of Zn in ZnO-ZFA was 19.24 wt% and clear peaks corresponding to Zn also appeared in SEM-EDX map (given in Fig. S1, Supplementary Material, SM), confirming the incorporation of this element to the modified FA material. The point of zero charge (PZC) of FA was 1.25 ± 0.38 mV and the ζ-potential at pH 4 was -19.1 ± 0.9 mV. The point of zero charge (PZC) of ZnO-ZFA was 6.06 ± 0.29, and the ζ-potential at pH 4 was +18.4 ± 0.6 mV. Therefore, at pH 4, ZA was charged negatively and ZnO-ZFA positively. The negative charge of FA was consistent with the usual isoelectric point of aluminosilicate minerals, typically below 4 as a consequence of the isomorphic substitution of Si^{4+} by Al^{3+} [29]. The higher PZC of ZnO-containing materials was due to the presence of ZnO, the PZC of which is > 9 [30]. The BET surface area increased from 5.98 $m^2\ g^{-1}$ for raw FA to 26.09 $m^2\ g^{-1}$ for ZnO-ZFA.

Table 1. Elemental composition of FA and ZnO-ZFA as determined by ICP-MS.

Element	FA (wt%)	ZnO-ZFA (wt%)
Aluminium	22.05	6.97
Iron	8.97	5.04
Calcium	5.24	3.18
Copper	0.01	0.01
Zinc	-	19.24
Manganese	2.44	0.04
Silicon	53.32	10.83
Titanium	1.07	0.44

The crystalline structure of the raw FA and ZnO-ZFA was investigated by XRD (Fig. 1). As shown in Fig. 1A, the predominant crystalline phase of FA was quartz (SiO_2, ICDD 00-003-0419), with minor contributions from nepheline ($Al_4KNa_3O_{16}Si_4$, ICDD 00-009-0458), Al_2O_3 (ICDD 00-003-1033), hematite (Fe_2O_3, ICDD 00-002-0915) and Ti_3O_5 (ICDD 00-027-0905). The alkaline hydrothermal process in the presence of $ZnCl_2$ promoted the formation of the hexagonal wurtzite structure of zinc oxide (ICSD 01-079-0206) and the SOD-type zeolite framework (sodalite octahydrate, $|Na_6(H2O)_8|[Si_6Al_6O_{24}]$) according to the database of zeolite structures IZA-SC (Fig. 1B). The diffraction peaks at 31.77°, 34.44°, 36.26°, 47.54°, 56.62°, 62.89°, 66.39°, 67.97°, 69.09° and 89.62° can be indexed to the (100), (002), (101), (102), (110), (103), (200), (112), (201) and (203) planes of wurtzite ZnO, while those exhibited at 14.05°, 24.44°, 31.77°, 35.17°, 42.99° and 58.50° can be attributed to the (110), (211), (310), (222), (411) and (440) planes of sodalite octahydrate, respectively.

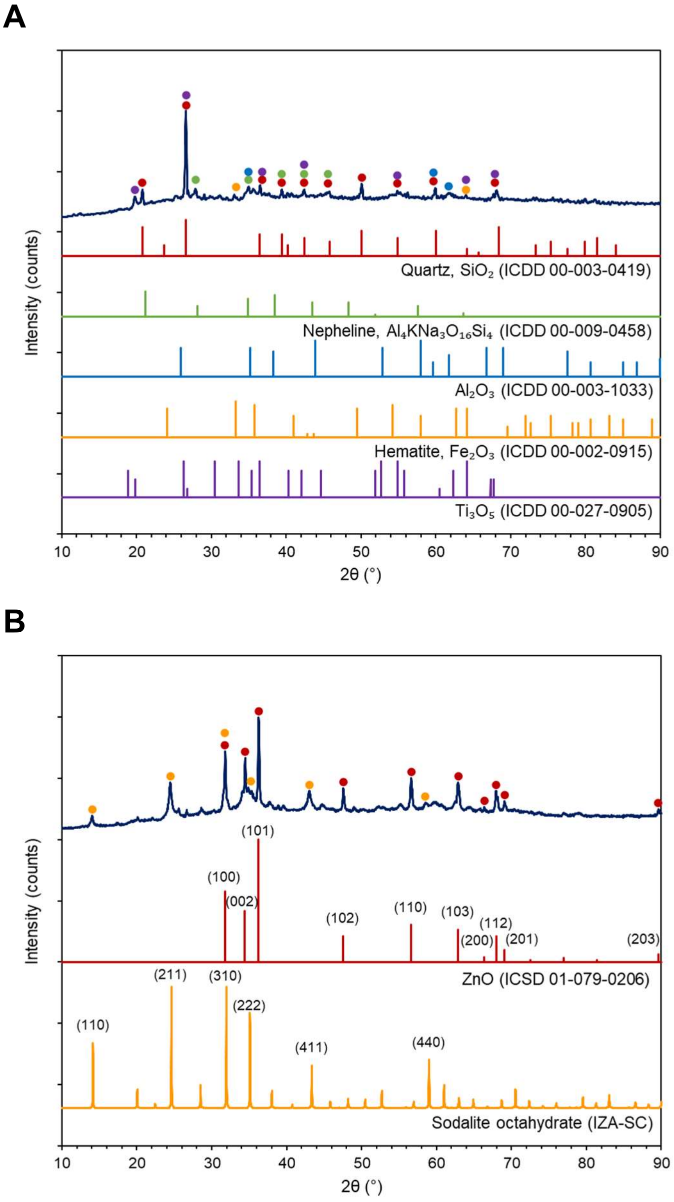

Figure 1. X-ray diffraction patterns of FA (A) and ZnO-ZFA (B) materials.

The optical properties of FA and ZnO-ZFA were evaluated by DRS (Fig. 2A). While no absorption edge was detected for FA, the characteristic absorption edge of ZnO in the UV region of the spectra was observed in the case of the zeolite material, corresponding to the promotion of electrons form valence to conduction band. The Kubelka-Munk function combined with Tauc's relation and baseline method was employed to calculate the band gap [31, 32], considering ZnO as a direct band gap semiconductor [33, 34]. The calculated band gap for ZnO-ZFA was 3.19 eV, in good agreement with previously reported values for ZnO [35-37].

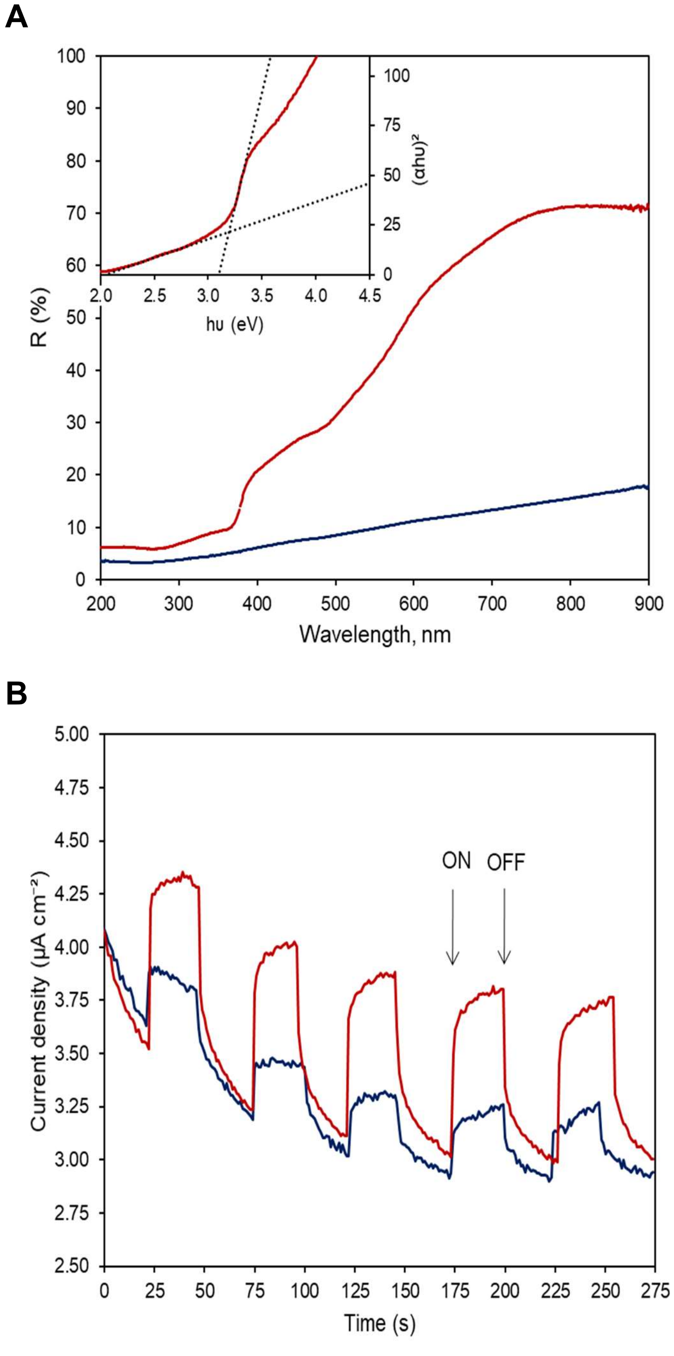

Figure 2. (A) UV-vis diffuse reflectance and Tauc's plots combined with baseline method of Kubelka-Munk function, and (B) transient photocurrent (TPC) responses at +1.0 V vs. Ag/AgCl in 0.1 M Na_2SO_4 under 365 nm UV light irradiation for ZnO-ZFA (red) and FA (blue).

To demonstrate the generation and effective separation of photoinduced electron-hole pairs, the transient photocurrent response was measured under chopped 365 nm light irradiation at +1.0 V vs. Ag/AgCl (Fig. 2B). During this process, a constant potential is applied to the working electrode and current is monitored over time. The current is the flow of electrons needed to support the active electrochemical processes at rates consistent with the potential. Therefore, the current of the electrode fluctuates according to the diffusion of an analyte from the bulk solution toward the sensor surface. The electroactive species present in the solution (analyte) in one oxidation state will be oxidized to another oxidation state. The oxidation will be diffusion-limited, thus causing the current to decrease to the base line (approaching zero) as this analyte is consumed [38]. Both materials exhibited anodic photocurrent under light irradiation, which could be attributed to the presence of photoactive metal oxides in the case of FA and photocatalytic ZnO for the zeolite material. The highest photocurrent density value was obtained for the ZnO-ZFA photocatalytic anodes, meaning a higher electron-hole pair generation and an improved charge carrier separation.

3.1.2. Characterization of ZnO-ZFA functionalized surfaces

Fig. 3 shows top-view SEM images of ZnO-ZFA spin-coated glass substrates. Apart from nanoparticle aggregates distributed over the entire surface of the substrate, larger particles scattered on the surface were clearly observed, which conferred a high surface roughness. The wettability of the ZnO-ZFA coatings before and after UV treatment resembling winter-fall, L(+), and summer-spring, L(++), irradiation was studied by WCA measurements. The WCA of glass substrates was 65.0 ± 0.4°, which did not change upon UV irradiation. The photocatalytic surface was hydrophilic, showing a WCA value of 66.4 ± 2.9°, and exhibited photoinduced hydrophilicity under UV irradiation, increasing their wettability after L(+) and L(++) irradiation to 61.9 ± 0.5° and 55.2 ± 1.1° respectively. The reason is that the photogenerated electron-hole pairs on the surface react with Zn-O lattice bonds, forming Zn+ defective sites and oxygen vacancies, which interact with water causing their dissociative adsorption [39-41].

TXRF analyses performed after 20 h contact with water at 37 ºC allowed evaluating the passing to the solution of the metals contained in functionalized coatings, which could be possibly related to the antimicrobial activity of functionalized surfaces (Fig. S2, SM). The results showed the presence of Zn^{2+} and Ca^{2+} ions with concentration markedly increasing during the first 2.5 hours, to slightly increase thereafter. Zn^{2+} ion concentration reached a value of 11 µg cm^{-2} or 4.5 mg L^{-1}, still below ZnO solubility limit [42]

3.2. Photocatalytic activity

3.2.1. Photocatalytic degradation of ciprofloxacin

Fig. 4A shows the changes of the absorbance spectrum of CIP during photocatalytic degradation by ZnO-ZFA. CIP was quantified using the wavelength of 277 nm as indicated before. The UV-vis absorption spectra of CIP showed a rapid decrease of the peaks at 277 and 330 nm during the first 5 min under 365 nm irradiation. In parallel, shoulders in the absorbance spectra appeared at 240-260 and 290 nm, which increased with irradiation time. After 20 min of irradiation the peaks at 277 and 330 nm, which identified CIP completely disappeared indicating the complete photocatalytic degradation of CIP by ZnO-ZFA. The UV absorbing intermediates were most probably the product of the attacks in the piperazinyl moiety, which preserved the quinolone moiety from ciprofloxacin, as shown elsewhere [43]. Pure ZnO show relatively low photocatalytic performance, about 26.9 %, after 60 min irradiation (Fig. 4C and E). Fig. 4D shows the concentration of CIP in non-catalytic runs showing that the degradation produced by photolysis was negligible. The negligible photolysis of CIP under 365 nm irradiation can be attributed to the fact that its maximum absorption takes place at 277 nm [44, 45]. Besides, at pH 4, with the carboxylic group not ionized and the basic nitrogen completely protonated, CIP presents its maximum stability [45]. Fig. 4E compares the performance of ZnO-ZFA and FA. The results showed that FA presented a high adsorption capacity for CIP, reaching 80 % removal after 120 min, but was unable to

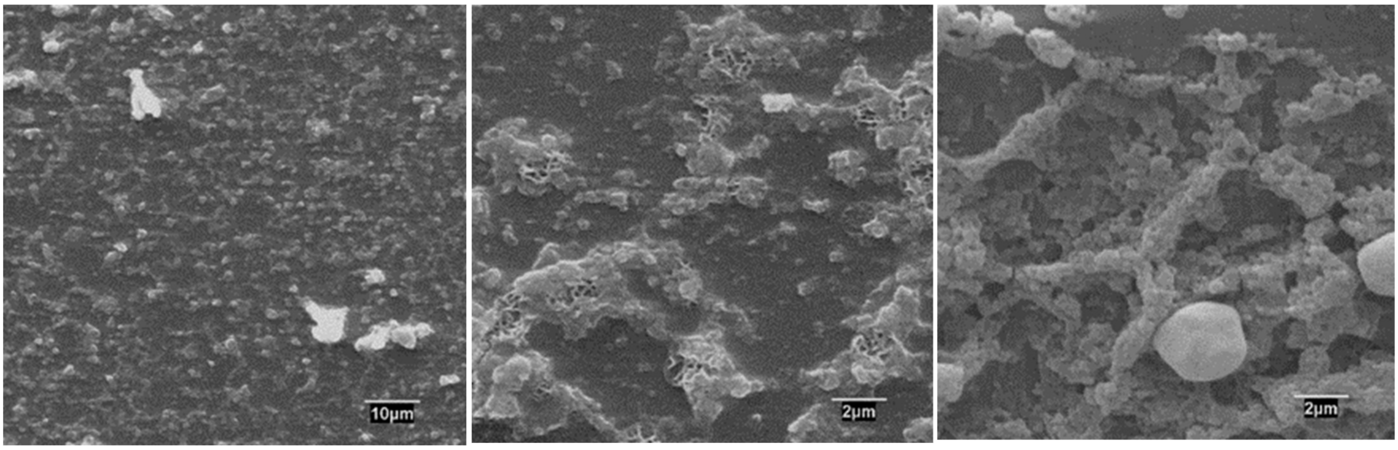

Figure 3. SEM images of ZnO-functionalized zeolite spin-coated glass substrates.

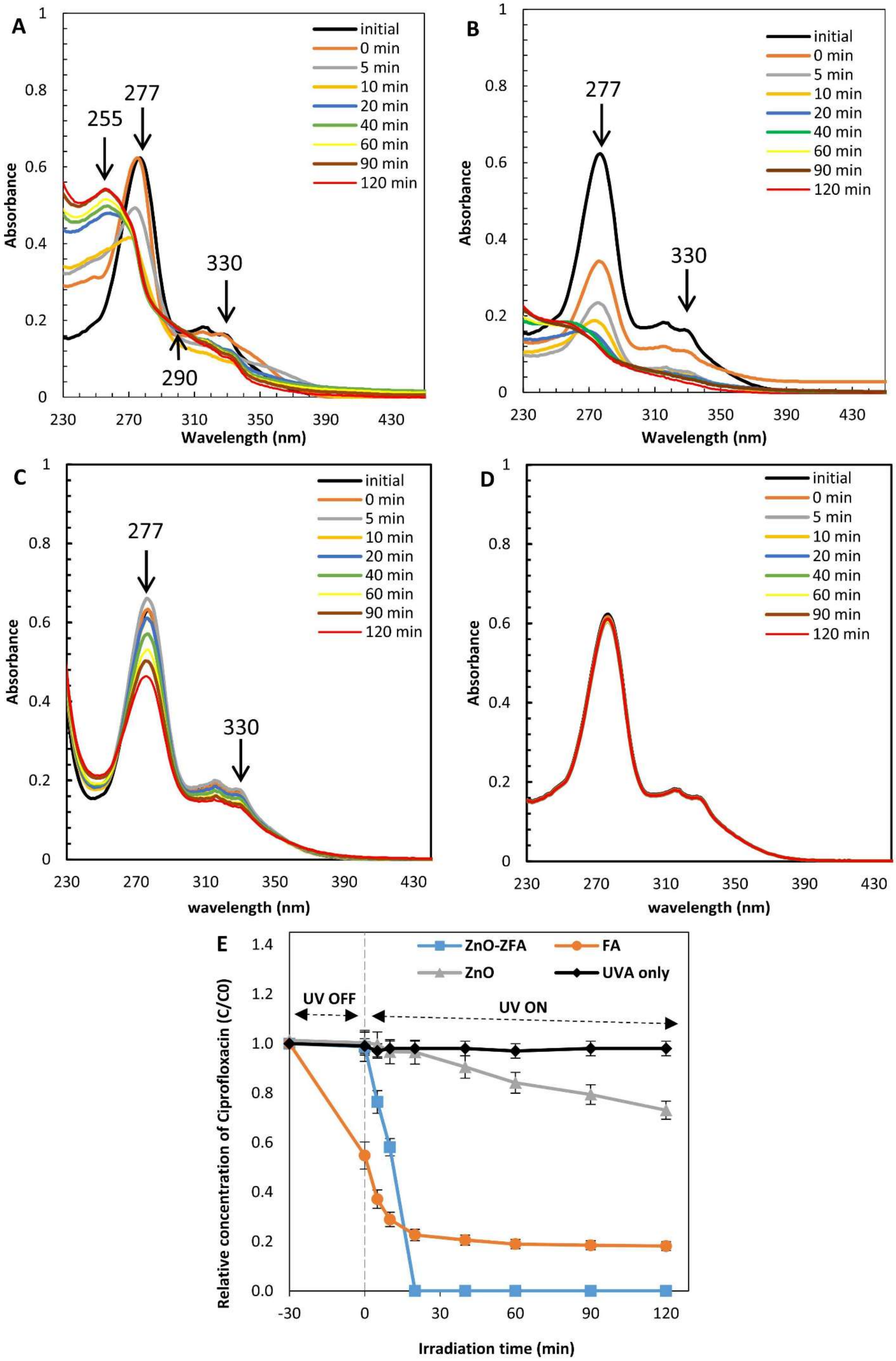

Figure 2. Degradation of CIP (10 mg/L, pH 4) at room temperature, under 365 nm UVA LED light irradiation. UV-vis absorption spectra (in the 230-440 nm interval) of CIF solution during photocatalytic degradation by ZnO-ZFA (A), FA (B), ZnO (C), and UVA only (photolysis) (D). CIP removal efficiency by ZnO-ZFA, FA, and ZnO (E).

completely remove CIP from solution. Besides, the absence of new peaks or shoulders, particularly those at 240-260 and 290 nm suggested that no photocatalytic degradation took place in the presence of FA. A maximum adsorption of ~1.3 % of the initial CIP or 0.020 mol CIP (g ZnO-ZFA)$^{-1}$ was observed during the 30 min of contact in the dark (before irradiation). The adsorption capacity of FA was much higher, reaching 0.85 mol CIP (g ZF)$^{-1}$, which could be attributed to the electrostatic interaction of the positively charged CIP and the negatively charged surface of FA at pH 4. CIP is a zwitterionic compound between pH 6.2 and 8.7 and is positively charged at pH 4 due to the protonation of the piperazinyl group [46].

El Kemary et al. (2010) studied the photodegradation of CIP using ZnO nanoparticles prepared using a precipitation method [20]. The material was active at 334 nm, only a slightly shorter wavelength than the band gap of our material ZnO-ZFA. ZnO nanoparticles displayed high photocatalytic activity for the degradation of CIP at basic pH (in the 7-10) but were less efficient at pH 4. The observed degradation reached between 18% (at pH 4) and 50 % (at pH 10) after 60 min. In our case, ZnO-ZFA completely removed CIP at pH 4 in 20 min, probably favoured by the stability of particle suspensions at acidic pH. It has been shown that the suspensions of ZnO nanoparticles tend to form stable and compact aggregates of primary particles that cannot be readily disaggregated even using sonication. The tendency is higher near the point of zero charge of ZnO [47]. During the photocatalytic degradation of CIP using anatase TiO_2 (Aeroxide P25), Van Doorslaer et al. (2011) found a positive relationship between degradation rate and the amount adsorbed onto the catalyst surface, which was in turn strongly pH-dependent and favoured at neutral pH [45]. An explanation consistent with the zwitterionic character of CIP is that the adsorption is higher when the molecule is positively charged, and the surface bears a negative charge, which happens for anatase P25 at pH > 6.2 [48]. Our photocatalytic material was able to degrade CIP even under conditions for which the surface was positively charged and avoiding the shortcomings of ZnO nanoparticle aggregation. As seen in Table S1, the ZnO-ZFA activated with 365 nm UVA-LED in the present study performed much better at acidic pH (pH 4) compared with the other photocatalytic materials and processes previously reported. Therefore, it can be concluded from this comparison that the as-prepared ZnO-ZFA is a promising catalyst under UVA irradiation.

3.2.2. Photodisinfection

Fig. 5 shows the bacterial concentration of *S. aureus* (Fig. 5A) and E. coli (Fig. 5B) during irradiated (60min, up to 2.0 kW-h m^{-2} summer-spring, L(++) irradiance) and non-irradiated (L(-)) runs in the presence of FA, ZnO, and ZnO-ZFA. The results are expressed as the logarithm of the concentration of colony forming cells and showed no significant effect of differences among treatments for runs carried out in the absence of irradiation and between them and control experiments performed without FA, ZnO or ZnO-ZFA. The absence of cell damage in non-irradiated runs carried out in the presence of ZnO-ZFA was attributed to the low concentration of dissolved Zn^{2+}, limited by ZnO solubility, which, as explained below, would be insufficient to interact with the cells and to inhibit bacterial growth during the 60 min contact time [49]. Also, no significant differences were observed in the number of viable colonies between irradiated and non-irradiated controls meaning that the 365 nm light did not impair the bacterial strains used in this work. However, a considerable decrease in the number of viable cells was observed for suspensions of ZnO-ZFA both in the case of *S. aureus* (3.65 ± 0.10 log-decrease) and *E. coli* (2.14 ± 0.20 log-decrease) during 60 min of UVA irradiation (2.0 kW-h m−2 summer-spring, L(++) irradiance). The bacterial inhibition obtained corresponded to the disinfection level achieved with the irradiation equivalent to a summer day. It is important to notice that bacteria were growing in optimum conditions of temperature and nutrient availability. The level of disinfection in real conditions is expected to be much higher (50). 1.84 ± 0.10 and 2.11 ± 0.05 log-decrease was observed for *S. aureus* after 60 min of contact with ZnO under dark L(-) and UVA irradiation (2.0 kW-h m^{-2} summer-spring, L(++) irradiance), respectively. The 0.27 ± 0.05 log difference between irradiated and non-irradiated indicated that the antibacterial activity of the pure ZnO was mainly attributed to the dissolved Zn^{2+} and/or direct contact with bacteria [49] and less to the photocatalytic process. The damage to *E. coli* was lower.

The higher activity of photocatalytic antimicrobial materials for *S. aureus* in comparison with *E. coli* is a common finding related to the different structures of the outer cell envelopes of Gram- positive and Gram-negative bacteria [51]. Contrasting results were also obtained. The difference between the components of Gram-positive and Gram-negative cell walls was described by Tayel et. al [52] and Reddy et al [53]. These authors suggested that Gram-positive bacteria are more sensitive to ZnO NPs than Gram-negative bacteria because the peptidoglycan layer that surrounds Gram-positive bacteria can promote ZnO attack inside the cell, while the cell wall components of Gram-negative bacteria, such as lipopolysaccharides, can counter this attack. The minimum inhibitory concentration of ZnO NPs founded in *S. aureus* and *E. coli* was 1 mg/mL and 3.4 mg/mL, respectively, which demonstrated that the inhibition of Gram-negative bacteria requires higher concentrations of ZnO NPs [53]. It has been showed that Gram-positive bacteria were more sensitive to peroxide hydrogen than Gram-negative bacteria when exposed to textiles containing ZnO NPs [54].

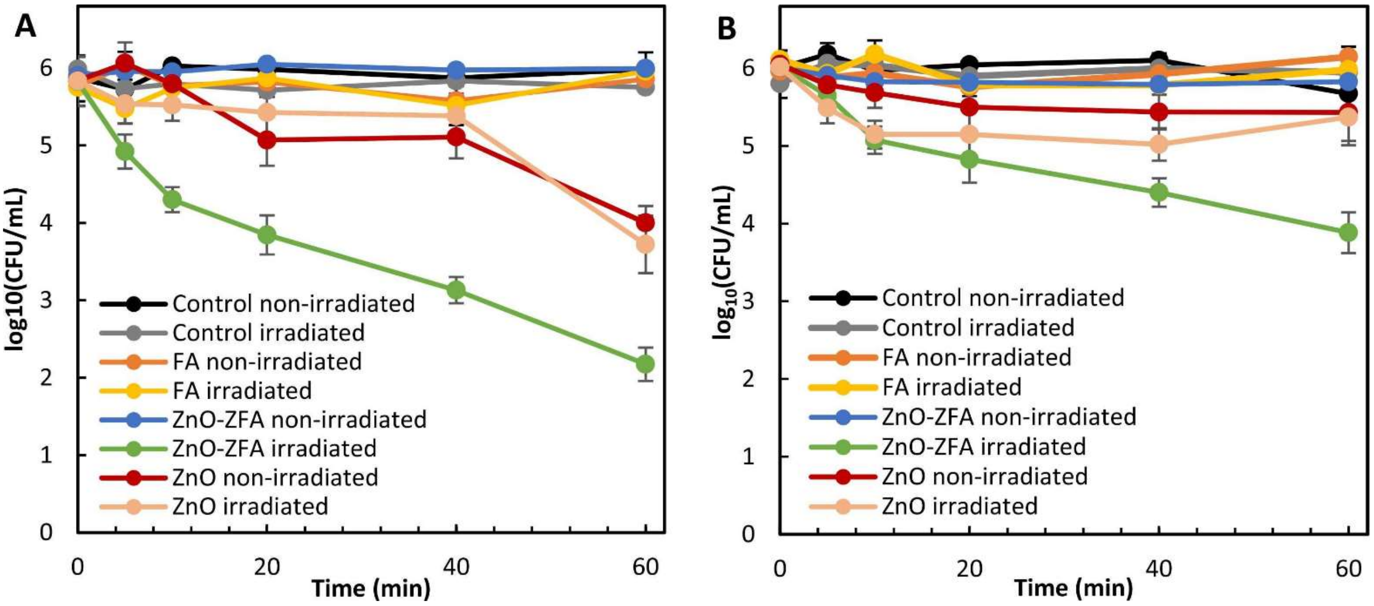

Figure 5. Colony forming units of *S. aureus* (A) and *E. coli* (B) cultures represented as the $\log_{10}$(CFU mL^{-1}) for UVA irradiated and non-irradiated, L(-), inactivation experiments in suspension using FA, ZnO, and ZnO-ZFA during 60 min (2.0 kW-h m^{-2} summer-spring, L(++) irradiance).

These results demonstrated the photocatalytic capacity of ZnO-ZFA to impair Gram-positive and Gram-negative bacteria as a consequence of high stability of the material and synergic action of the metallic oxides from the precursors.

The photocatalytic efficiency of functionalized surfaces (1 cm^2) after spin coating with ZnO-ZFA was investigated by quantifying the reduction of viable colonies of *S. aureus* and *E. coli* in surfaces and in the liquid in contact with them. Prior to irradiation, an incubation period of 20 h at 37 °C in the dark was allowed to obtain a mature biofilm on the surface of specimens. No inhibition of bacterial cells in liquid was observed during incubation with uncoated glass samples (Fig. 6A1 and 6B1). The results showed a log-reduction of CFU counts of 1.53 ± 0.22 log and 1.39 ± 0.13. for *S. aureus* (Fig. 6A1) and *E. coli* (Fig. 6B1) cultures in the dark. The limited inhibitory effect of ZnO-functionalized material against planktonic cells in the absence of UVA irradiation could be attributed to the release of dissolved zinc ions to the solution. As shown in Fig. S2 (SM), the concentration of Zn2+ released from the photocatalytic coatings reached 11 µg cm^{-2} (corresponding to a concentration of 4.5 mg L^{-1}) after 20 h. This result agrees with data shown elsewhere showing the impairment of S. aureus cells viability after contact with ZnO-electrosprayed coatings in the dark. Valenzuela et al. (2019) obtained a 5-6-log reduction of *S. aureus* viable colonies 20 h contact with ZnO electrosprayed coatings releasing Zn^{2+} up to a concentration of 6.7 mg L^{-1} [19]. The role played by zinc dissolution in different ZnO-containing materials is a well-known fact [55]. The damage to different cellular components caused by Zn^{2+} ions and their inhibition levels to different bacteria has been also shown elsewhere [56-58]. The results presented in Fig. 6 showed that ZnO-ZFA coatings were capable of completely avoiding the growth of *S. aureus* and inhibiting the formation of new *E. coli* colonies by 4-5 orders or magnitude. The higher activity of photocatalytic antimicrobial materials for *S. aureus* in comparison with *E. coli* is a common finding related to the different structures of the outer cell envelopes of Gram- positive and Gram-negative bacteria [51-54] . In addition, ZnO-ZFA coatings maintained the antibacterial and anti-fouling capacities upon 4 cycles of usage against *S. aureus* (Fig. S3) and *E. coli* (Fig. S4) without losing their integrity (Fig. S5). No statistically significant decline in the disinfection efficiency was observed for organic fouled ZnO-ZFA coatings compared to the clean ZnO-ZFA coatings (Fig. S6), probably due to the low attachment of the protein BSA to the surface (Fig. S7).

Fig. 7 shows the generation of ROS in bacterial cells in contact with FA and ZnO-ZFA in suspension (Fig. 7A1-A2) and coatings (Fig. 7B1-B2). Bacterial suspensions irradiated in the absence of the tested materials and with FA exposed to UVA light presented not significant (< 5 %) variation in ROS levels with respect to dark controls. However, ZnO-ZFA yielded a considerable level of ROS under UVA, 365 nm light irradiation, which increased with exposure time either for the case of material in suspension and for coatings. Interestingly, the level of ROS produced in both bacterial strains by ZnO-ZFA was higher for coatings than for suspensions (almost twice after 60 min of irradiation), a result that could be explained by the absorption of light in the case of powdered materials in suspension that that reduce the penetration of light and the photocatalytic activity [59]. Overall, the generation of ROS exhibits the same pattern than bacterial impairment (Figs. 5 and 6). The incident photon energy

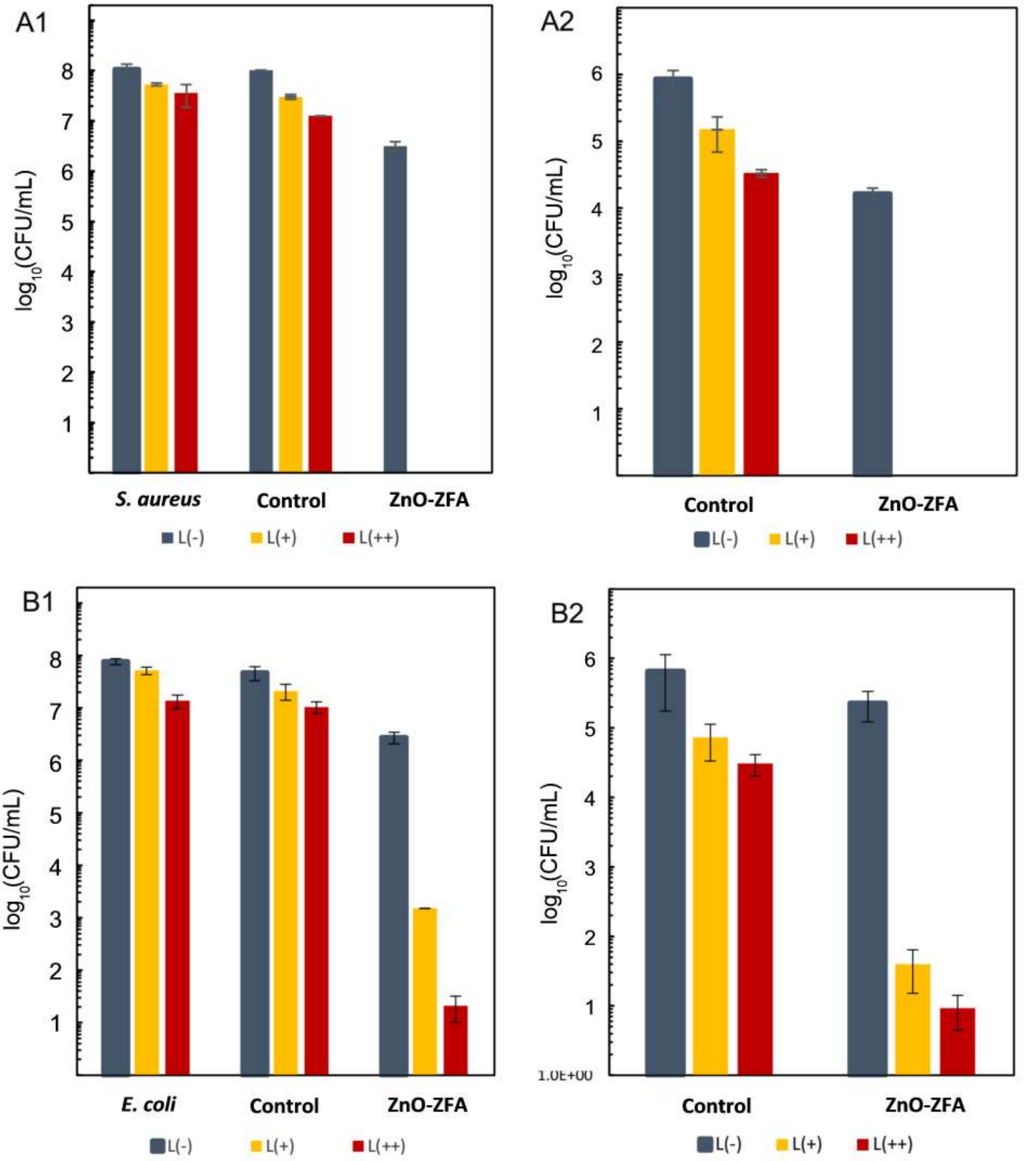

Figure 6. Colony forming units represented as $\log_{10}$(CFU mL^{-1}) for cultures of *S. aureus* (A) and *E. coli* (B) in contact with uncoated and ZnO-ZFA glass substrates after biofilm growth for 20 h in dark, L(–), and subsequent 365 nm irradiation mimicking winter-fall, L(+), and summer-spring, L(++) irradiances. A1 and B1 show CFU of bacterial cells in suspension (planktonic bacteria) while A2 and B2 CFU represent biofilm detached from the surface (sessile bacteria). Controls of both S. aureus and E. coli are also shown.

for the 365 nm light is 3.4 eV, which is close to the band gap of ZnO-FFA (3.2 eV). Therefore, electrons in ZnO-ZFA structure can be photoexcited with subsequent generation of different types of biologically active ROS [60]. The formation of radicals such as $O_2^{\cdot -}$, $HO^{\cdot}$ and H_2O_2 is usually considered one of the main ROS mechanisms for zinc as well as for titanium, iron, aluminium, copper or manganese oxide -related materials [19, 61, 62]. These results demonstrated that the inactivation of pathogens by ZnO-ZFA was due to the ROS generated under UVA irradiation and, to a lower extent, to the effect of dissolved Zn^{2+}. The oxidative stress generated at the ZnO-ZFA interface under 365nm UVA light resulted in 83% and 61% cell membrane damage on *S. aureus* and *E. coli*, respectively (Fig. S8), leading to bacterial cell death

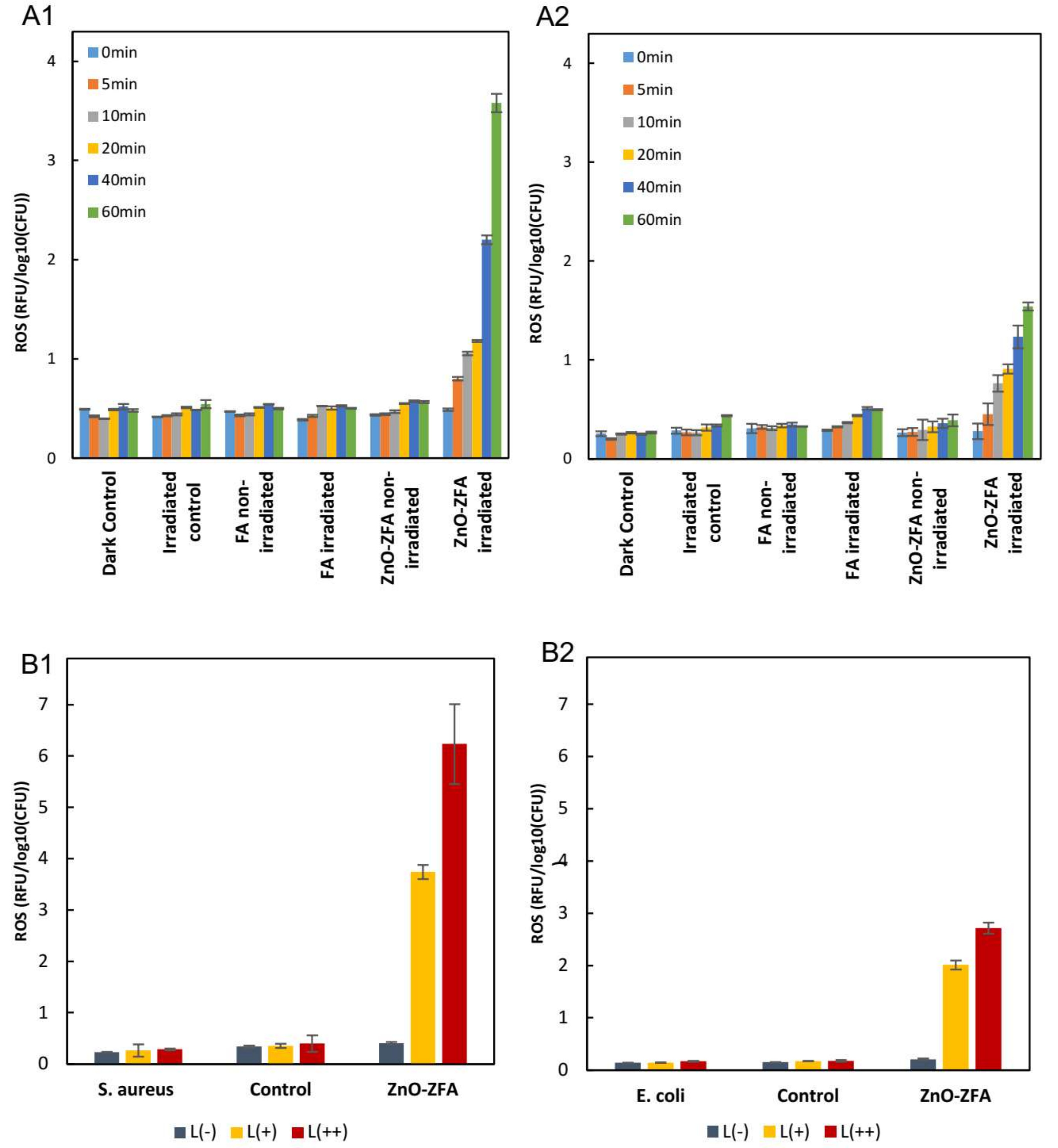

Figure 7. Oxidative stress express in term of ROS (DCF) for *S. aureus* (A1-B1) and *E. coli* (A2-B2), under 365 nm UVA irradiation with: (A) suspensions of FA and ZnO-FA (for 0, 5, 10, 20, 40, 60 min); and (B) coatings of ZnO-ZFA previously incubated in the dark for 24h: L(-): without irradiation; L(+): 1.0 kW-h m^{-2} (winter-fall); and L(++): 2.0 kW-h m^{-2} (summer-spring).

Moreover, the potential toxicity or health hazards of engineered nanomaterials is one of the crucial aspects associated with their real-life applications [63]. In this work, we studied the cytotoxicity of ZnO-FA against hDF, which are the first-line barrier between the internal organs and external environment [64]. Fig. S9 (SM) shows the results of MTT assay using three concentrations of ZnO-ZFA (10, 100, and 1000 mg L^{-1}). The results demonstrated that ZnO-ZFA produced low cytotoxicity to hDF, with a maximum viability inhibition of 19.8 ± 0.1 % at the very high concentration of 1000 mg L^{-1}. Overall, our results showed that zeolitic ZnO-ZFA prepared from raw FA was active against a variety of bacteria due to its UVA-driven photocatalytic activity but are non-toxic to human cells even at much higher concentrations than those required for antimicrobial activity.

4. Conclusions

In this work, we prepared a zeolitic material using a combustion fly ash from the electrostatic precipitator of a commercial power plant. The raw material was modified by incorporating ZnO by means of an alkaline hydrothermal method. The prepared material, ZnO-ZFA, displayed the zeolitic structure of sodalite and was tested for the photocatalytic removal of the antibiotic CIP and the inactivation of gram-positive and gram-negative bacteria. The zeolitic material ZnO-ZFA displayed a band-gap of 3.2 eV and transient photocurrent response that demonstrated the effective separation of photoinduced electron-hole pairs when irradiated by 365 nm UVA light. The results showed that CIP could be completely degraded in less than 20 min at pH 4 using an irradiation power of 5.1 W L^{-1}.

The material ZnO-ZFA displayed high antimicrobial activity on *S. aureus* and *E. coli* bacteria, either in suspensions or in photocatalytic surfaces prepared by spin-coating functionalization of glass substrates. The results showed that ZnO-ZFA coatings were able to completely avoid the growth of *S. aureus* for UVA doses as low as 1.0 and 2.0 kW-h m^{-2} and reduced the formation of *E. coli* colonies on functionalized surfaces by about 4 orders of magnitude.

The impairment of bacterial cell was essentially due to the light-driven overproduction of ROS, with a limited effect of Zn^{2+} dissolution. The zeolitic material ZnO-ZFA was non-toxic for human fibroblasts at concentration as high as 1 g L^{-1}.

The preparation of functionalized zeolitic material ZnO-ZFA by classic alkaline hydrothermal synthesis and spin-coating allows for scalability and potential application for (photo)disinfection, anti-fouling, and (photo)degradation uses.

Acknowledgements

GA and MV thank to ICDT of Transilvania University Brașov (RESREC Research Institute). AIJ, LV and RR thank Fundación Ramón Areces (project OTR02666-20172353).

References

[1] R.P. Girón, B. Ruiz, E. Fuente, R.R. Gil, I. Suárez-Ruiz, Properties of fly ash from forest biomass combustion, Fuel 114 (2013) 71-77. https://doi.org/10.1016/j.fuel.2012.04.042.

[2] Z.T. Yao, X.S. Ji, P.K. Sarker, J.H. Tang, L.Q. Ge, M.S. Xia, Y.Q. Xi, A comprehensive review on the applications of coal fly ash, Earth-Sci. Rev. 141(2015) 105-121. https://doi.org/10.1016/j.earscirev.2014.11.016.

[3] C. Ferreira, A. Ribeiro, L. Ottosen, Possible applications for municipal solid waste fly ash, J. Hazard. Mater. 96 (2003) 201-216. https://doi.org/10.1016/S0304-3894(02)00201-7.

[4] K.M. Zierold, C. Odoh, A review on fly ash from coal-fired power plants: chemical composition, regulations, and health evidence, Rev. Environ. Health. 35 (2020) 401-418. https://doi.org/10.1515/reveh-2019-0039.

[5] S. Laohaprapanon, M. Marques, W. Hogland, Removal of organic pollutants from wastewater using wood fly ash as a low-cost sorbent, Clean-Soil, Air, Water 38 (2010) 1055-1061. https://doi.org/10.1002/clen.201000105.

[6] V. Gadore, M. Ahmaruzzaman, Fly ash–based nanocomposites: a potential material for effective photocatalytic degradation/elimination of emerging organic pollutants from aqueous stream, Environ. Sci. Pollut. Res. 28 (2021) 46910-46933. https://doi.org/10.1007/s11356-021-15251-0.

[7] P. Huo, Y. Yan, S. Li, H. Li, W. Huang, Floating photocatalysts of fly-ash cenospheres supported AgCl/TiO_2 films with enhanced Rhodamine B photodecomposition activity, Desalination 256 (2010) 196-200. https://doi.org/10.1016/j.desal.2010.01.012.

[8] J. Zhang, H. Cui, B. Wang, C. Li, J. Zhai, Q. Li, Fly ash cenospheres supported visible-light-driven BiVO4 photocatalyst: Synthesis, characterization and photocatalytic application, Chem. Eng. J. 223 (2013) 737-746. https://doi.org/10.1016/j.cej.2012.12.065.

[9] B. Pant, G. P. Ojha, H.-Y. Kim, M. Park, S.-J. Park, Fly-ash-incorporated electrospun zinc oxide nanofibers: Potential material for environmental remediation. Environ. Pollut. 245 (2019) 163-172. https://doi.org/10.1016/j.envpol.2018.10.122.

[10] M. Visa. Tailoring fly ash activated with bentonite as adsorbent for complex wastewater treatment, Appl. Surf. Sci. 263 (2012) 753-762. https://doi.org/10.1016/j.apsusc.2012.09.156.

[11] L. Yang, F. Wang, A. Hakki, D. E. Macphee, P. Liu, S. Hu, The influence of zeolites fly ash bead/TiO_2 composite material surface morphologies on their adsorption and photocatalytic performance, Appl. Surf. Sci. 392 (2017) 687-696. https://doi.org/10.1016/j.apsusc.2016.09.023.

[12] W. Franus, M. Wdowin, M. Franus, Synthesis and characterization of zeolites prepared from industrial fly ash, Environ. Monit. Assess. 186 (2014) 5721-5729. https://doi.org/10.1007/s10661-014-3815-5.

[13] N. Sakai, A. Fujishima, T. Watanabe, K. Hashimoto, Quantitative evaluation of the photoinduced hydrophilic conversion properties of TiO_2 thin film surfaces by the reciprocal of contact angle, J. Phys. Chem. B 107 (2003) 1028-1035. https://doi.org/10.1021/jp022105p.

[14] A.V. Rudakova, A.V. Emeline, D.W. Bahnemann, Effect of the TiO_2–ZnO heterostructure on the photoinduced hydrophilic conversion of TiO_2 and ZnO surfaces, J. Phys. Chem. C 123 (2019) 8884-8891. https://doi.org/10.1021/acs.jpcc.8b12125.

[15] K. Nakata, A. Fujishima, TiO_2 photocatalysis: Design and applications, J. Photochem. Photobiol.

C: Photochem. Rev. 13 (2012) 169-189. https://doi.org/10.1016/j.jphotochemrev.2012.06.001.

[16] Y. Yan, X. Zhou, J. Lan, Z. Li, T. Zheng, W. Cao, N. Zhu, W. Liu, Efficient photocatalytic disinfection of *Escherichia coli* by N-doped TiO_2 coated on coal fly ash cenospheres, J. Photochem. Photobiol. A 367 (2018) 355-364. https://doi.org/10.1016/j.jphotochem.2018.08.045.

[17] S. Tuntachon, K. Kamwilaisak, T. Somdee, W. Mongkoltanaruk, V. Sata, K. Boonserm, A. Wongsa, P. Chindaprasirt, Resistance to algae and fungi formation of high calcium fly ash geopolymer paste containing TiO_2, J. Build. Eng. 25 (2019) 100817. https://doi.org/10.1016/j.jobe.2019.100817.

[18] M. Visa, Synthesis and characterization of new zeolite materials obtained from fly ash for heavy metals removal in advanced wastewater treatment, Powder Technol. 294 (2016) 338-347. https://doi.org/10.1016/j.powtec.2016.02.019.

[19] L. Valenzuela, A. Iglesias, M. Faraldos, A. Bahamonde, R. Rosal, Antimicrobial surfaces with self-cleaning properties functionalized by photocatalytic ZnO electrosprayed coatings, J. Hazard. Mater. 369 (2019) 665-673. https://doi.org/10.1016/j.jhazmat.2019.02.073.

[20] M. El-Kemary, H. El-Shamy, I. El-Mehasseb, Photocatalytic degradation of ciprofloxacin drug in water using ZnO nanoparticles, J. Lumin. 130 (2010) 2327-2331. https://doi.org/10.1016/j.jlumin.2010.07.013.

[21] ISO 22196, Measurement of antibacterial activity on plastics and other non-porous surfaces. (2011).

[22] A. Gomes, E. Fernandes, J.L.F.C. Lima, Fluorescence probes used for detection of reactive oxygen species, J. Biochem. Bioph. Methods 65 (2005) 45-80. https://doi.org/10.1016/j.jbbm.2005.10.003.

[23] B. Kalyanaraman, V. Darley-Usmar, K.J.A. Davies, P.A. Dennery, H. J. Forman, M.B. Grisham, G.E. Mann, K. Moore, L.J. Roberts, H. Ischiropoulos, Measuring reactive oxygen and nitrogen species with fluorescent probes: challenges and limitations, Free Radic. Biol. Med. 52 (2012) 1-6. https://doi.org/10.1016/j.freeradbiomed.2011.09.030.

[24] H. Shu, H. Chen, X. Wang, Y. Hu, Y. Yun, Q. Zhong, W. Chen, W. Chen, Antimicrobial Activity and Proposed Action Mechanism of 3-Carene against *Brochothrix thermosphacta* and *Pseudomonas fluorescens*. Molecules 24 (2019). https://doi.org/10.3390/molecules24183246.

[25] J. Santiago-Morales, G. Amariei, P. Leton, R. Rosal, Antimicrobial activity of poly(vinyl alcohol)-poly(acrylic acid) electrospun nanofibers. Colloids Surf. B. 146 (2016)144-151. https://doi.org/10.1016/j.colsurfb.2016.04.052.

[26] B. Jalvo, M. Faraldos, A. Bahamonde, R. Rosal, Antibacterial surfaces prepared by electrospray coating of photocatalytic nanoparticles. Chem. Eng. J. 334 (2018) 1108-1118. https://doi.org/10.1016/j.cej.2017.11.057.

[27] B. Díez, G. Amariei, R. Rosal, Electrospun composite membranes for fouling and biofouling control. Ind. Eng. Chem. Res. 57 (2018) 14561-14570. https://doi.org/10.1021/acs.iecr.8b04011.

[28] ASTM C618-19, Standard Specification for Coal Fly Ash and Raw or Calcined Natural Pozzolan for Use in Concrete, ASTM International, West Conshohocken, PA, www.astm.org. (2019).

[29] A. Kumar, C. Marcolli, T. Peter, Ice nucleation activity of silicates and aluminosilicates in pure water and aqueous solutions–Part 3: Aluminosilicates. Atmos. Chem. Phys. 19 (2019) 6059-6084. https://doi.org/10.5194/acp-19-6059-2019.

[30] D. Zhou, A. A. Keller, Role of morphology in the aggregation kinetics of ZnO nanoparticles, Water Res. 44 (2010) 2948-2956. https://doi.org/10.1016/j.watres.2010.02.025.

[31] A. Escobedo-Morales, L. Ruiz, II, M.D. Ruiz-Peralta, L. Tepech-Carrillo, M. Sanchez-Cantu, J. E. Moreno-Orea, Automated method for the determination of the band gap energy of pure and mixed powder samples using diffuse reflectance spectroscopy, Heliyon 5 (2019) e01505. https://doi.org/10.1016/j.heliyon.2019.e01505.

[32] P. Makula, M. Pacia, W. Macyk, How to correctly determine the band gap energy of modified semiconductor photocatalysts based on UV-vis spectra, J. Phys. Chem. Lett. 9 (2018) 6814-6817. https://doi.org/10.1021/acs.jpclett.8b02892.

[33] X. Chen, S. Shen, L. Guo, S. S. Mao, Semiconductor-based photocatalytic hydrogen generation, Chem. Rev. 110 (2010) 6503–6570. https://doi.org/10.1021/cr1001645.

[34] E.M. Patterson, C.E. Shelden, B.H. Stockton, Kubelka-Munk optical properties of a barium sulfate white reflectance standard, Appl. Opt. 16 (1977) 729-732. https://doi.org/10.1364/AO.16.000729.

[35] P.K. Mishra, H. Mishra, A. Ekielski, S. Talegaonkar, B. Vaidya, Zinc oxide nanoparticles: a promising nanomaterial for biomedical applications, Drug Discov. Today 22 (2017) 1825-1834. https://doi.org/10.1016/j.drudis.2017.08.006.

[36] A. Krol, P. Pomastowski, K. Rafinska, V. Railean-Plugaru, B. Buszewski, Zinc oxide nanoparticles: Synthesis, antiseptic activity and toxicity mechanism, Adv. Colloid. Interface Sci. 249 (2017) 37-52. https://doi.org/10.1016/j.cis.2017.07.033.

[37] A. Sirelkhatim, S. Mahmud, A. Seeni, N. H. M. Kaus, L. C. Ann, S. K. M. Bakhori, H. Hasan, D. Mohamad, Review on zinc oxide nanoparticles: Antibacterial activity and toxicity mechanism,

Nano-Micro Lett. 7 (2015) 219-242. https://doi.org/10.1007/s40820-015-0040-x.

[38] A. J. Bard, L. R. Faulkner, Electrochemical Methods: Fundamentals and Applications. New York: Wiley, 2nd ed. Russian Journal of Electrochemistry 38 (2002) 1364–1365. https://doi.org/10.1023/A:1021637209564.

[39] S. Karuppuchamy, S. Ito, Cathodic electrodeposition of nanoporous ZnO thin films from new electrochemical bath and their photoinduced hydrophilic properties, Vacuum 82 (2008) 547-550. https://doi.org/10.1016/j.vacuum.2007.06.002.39.

[40] V. Khranovskyy, T. Ekblad, R. Yakimova, L. Hultman, Surface morphology effects on the light-controlled wettability of ZnO nanostructures, Appl. Surf. Sci. 258 (2012) 8146-8152. https://doi.org/10.1016/j.apsusc.2012.05.011.

[41] R.-D. Sun, A. Nakajima, A. Fujishima, T. Watanabe, K. Hashimoto, Photoinduced surface wettability conversion of ZnO and TiO_2 thin films, J. Phys. Chem. B 105 (2001) 1984–1990. https://doi.org/10.1021/jp002525j.

[42] C.A. David, J. Galceran, C. Rey-Castro, J. Puy, E. Companys, J. Salvador, J. Monné, R. Wallace, A. Vakourov, Dissolution kinetics and solubility of ZnO nanoparticles followed by AGNES, J. Phys. Chem. C 116 (2012) 11758-11767. https://doi.org/10.1021/jp301671b.

[43] N. Wachter, J.M. Aquino, M. Denadai, J.C. Barreiro, A.J. Silva, Q.B. Cass, R.C. Rocha-Filho, N. Bocchi, Optimization of the electrochemical degradation process of the antibiotic ciprofloxacin using a double-sided beta-PbO_2 anode in a flow reactor: kinetics, identification of oxidation intermediates and toxicity evaluation. Environ. Sci. Pollut. Res. 26 (2019) 4438-4449. https://doi.org/10.1007/s11356-018-2349-8.

[44] H.-S. Ou, J.-S. Ye, S. Ma, C.-H. Wei, N.-Y. Gao, J.-Z. He, Degradation of ciprofloxacin by UV and UV/H_2O_2 via multiple-wavelength ultraviolet light-emitting diodes: Effectiveness, intermediates and antibacterial activity, Chem. Eng. J. 289 (2016) 391-401 https://doi.org/10.1016/j.cej.2016.01.006.

[45] X. Van Doorslaer, K. Demeestere, P.M. Heynderickx, H. Van Langenhove, J. Dewulf, UV-A and UV-C induced photolytic and photocatalytic degradation of aqueous ciprofloxacin and moxifloxacin: Reaction kinetics and role of adsorption, Appl. Catal. B: Environ. 101 (2011) 540-547. https://doi.org/10.1016/j.apcatb.2010.10.027.

[46] J. Sun, S. Sakai, Y. Tauchi, Y. Deguchi, J. Chen, R. Zhang, K. Morimoto, Determination of lipophilicity of two quinolone antibacterials, ciprofloxacin and grepafloxacin, in the protonation equilibrium, Eur. J. Pharm. Biopharm. 54 (2002) 51-58. https://doi.org/10.1016/S0939-6411(02)00018-8.

[47] M.O. Fatehah, H.A. Aziz, S. Stoll, Stability of ZnO nanoparticles in solution. Influence of pH, dissolution, aggregation and disaggregation effects, J. Colloid Sci. Biotechnol. 3 (2014) 75-84. https://doi.org/10.1166/jcsb.2014.1072.

[48] K. Suttiponparnit, J. Jiang, M. Sahu, S. Suvachittanont, T. Charinpanitkul, P. Biswas, Role of aurface area, primary particle size, and crystal phase on titanium dioxide nanoparticle dispersion properties, Nanoscale Res. Lett. 6 27 (2010). https://doi.org/10.1007/s11671-010-9772-1.

[49] T.W. Turney, M.B. Duriska, V. Jayaratne, A. Elbaz, S.J. O'Keefe, A.S. Hastings, T.J. Piva, P.F. A. Wright, B.N. Feltis, Formation of zinc-containing nanoparticles from Zn^{2+} ions in cell culture media: implications for the nanotoxicology of ZnO, Chem. Res. Toxicol. 25 (2012) 2057-2066. https://doi.org/10.1021/tx300241q.

[50] K. Skowron, E. Walecka-Zacharska, K. Grudlewska, P. Gajewski, N. Wiktorczyk, M. Wietlicka-Piszcz, A. Dudek, K. J. Skowron, E. Gospodarek-Komkowska, Disinfectant susceptibility of biofilm formed by *Listeria monocytogenes* under selected environmental conditions. Microorganisms 7 (2019). https://doi.org/10.3390/microorganisms7090280.

[51] B. Lallo-da-Silva, M.P. Abucafy, E. Berbel Manaia, J.A. Oshiro, B.G. Chiari-Andreo, R.C.R. Pietro, L.A. Chiavacci, Relationship between structure and antimicrobial activity of zinc oxide nanoparticles: an overview. Int. J. Nanomedicine 14 (2019) 9395-9410. https://doi.org/10.2147/IJN.S216204.

[52] A.A. Tayel, W.F. El-Tras, S. Moussa, A.F. El-Baz, H. Mahrous, M.F. Salem, L. Brimer, Antibacterial action of zinc oxide nanoparticles against foodborne pathogens. J. Food Saf. 31 (2011) 211-218. https://doi.org/10.1111/j.1745-4565.2010.00287.x.

[53] K.M. Reddy, K. Feris, J. Bell, D.G. Wingett, C. Hanley, A. Punnoose, Selective toxicity of zinc oxide nanoparticles to prokaryotic and eukaryotic systems. Appl. Phys. Lett. 90 (2007) 2139021-2139023. https://doi.org/10.1063/1.2742324.

[54] R. Borda, R. Branquinho, M.P. Duarte, E. Maurício, A.L. Fernando, R. Martins, E. Fortunato, Efficient coverage of ZnO nanoparticles on cotton fibres for antibacterial finishing using a rapid and low cost in situ synthesis. New J. Chem. 42 (2018) 1052-1060. https://doi.org710.1039/c7nj03418k.

[55] H. Ma, P.L. Williams, S.A. Diamond, Ecotoxicity of manufactured ZnO nanoparticles –A review. Environ. Pollut. 172 (2013) 76-85. https://doi.org/10.1016/j.envpol.2012.08.011.

[56] B.A. Holt, S.A. Gregory, T. Sulchek, S. Yee, M. D. Losego, Aqueous zinc compounds as residual antimicrobial agents for textiles. ACS Appl. Mater. Interfaces 10 (2018) 7709-7716. https://doi.org/10.1021/acsami.7b15871.

[57] J. Pasquet, Y. Chevalier, J. Pelletier, E. Couval, D. Bouvier, M.-A. Bolzinger, The contribution of zinc ions to the antimicrobial activity of zinc oxide, Colloids Surf. A Physicochem. Eng. Asp. 457 (2014) 263-274. https://doi.org/10.1016/j.colsurfa.2014.05.057.

[58] M. Premanathan, K. Karthikeyan, K. Jeyasubramanian, G. Manivannan, Selective toxicity of ZnO nanoparticles toward Gram-positive bacteria and cancer cells by apoptosis through lipid peroxidation, Nanomedicine 7 (2011) 184-192. https://doi.org/10.1016/j.nano.2010.10.001.

[59] A. Tolosana-Moranchel, C. Pecharromán, M. Faraldos, A. Bahamonde, Strong effect of light scattering by distribution of TiO_2 particle aggregates on photocatalytic efficiency in aqueous suspensions, Chem. Eng. J. 403 (2021) 126186. https://doi.org/10.1016/j.cej.2020.126186.

[60] Y. Li, J. Niu, W. Zhang, L. Zhang, E. Shang, Influence of aqueous media on the ROS-mediated toxicity of ZnO nanoparticles toward green fluorescent protein-expressing *Escherichia coli* under UV-365 irradiation, Langmuir 30 (2014) 2852-2862. https://doi.org/10.1021/la5000028.

[61] N. Sharma, S. Jandaik, S. Kumar, M. Chitkara, I. S. Sandhu, Synthesis, characterisation and antimicrobial activity of manganese- and iron-doped zinc oxide nanoparticles. J. Exp. Nanosci. 11 (2015) 54-71. https://doi.org/10.1080/17458080.2015.1025302.

[62] V. Stanić, S.B. Tanasković, Antibacterial activity of metal oxide nanoparticles. (2020) 241-274. https://doi.org/10.1016/b978-0-12-819943-5.00011.

[63] D. Bagchi, A. Bhattacharya, T. Dutta, S. Nag, D. Wulferding, P. Lemmens, S.K. Pal, Nano MOF entrapping hydrophobic photosensitizer for dual-stimuli-responsive unprecedented therapeutic action against drug-resistant bacteria, ACS Appl. Bio Mater. 2 (2019) 1772-1780. https://doi.org/10.1021/acsabm.9b00223.

[64] B. Drasler, P. Sayre, K.G. Steinhäuser, A. Petri-Fink, B. Rothen-Rutishauser, In vitro approaches to assess the hazard of nanomaterials. NanoImpact 8 (2017) 99-116. https://doi.org/10.1016/j.impact.2017.08.002.

Supplementary Material

ZnO-functionalized fly-ash based zeolite for ciprofloxacin antibiotic degradation and pathogen inactivation

Georgiana Amariei[1,2,‡,*], Laura Valenzuela[2,‡], Ana Iglesias-Juez[3], Roberto Rosal[2], Maria Visa[4]

[1] Department of Biological and Chemical Engineering- Plastic and Polymer Engineering Group, Aarhus University, Aabogade 40, DK-8200, Aarhus N., Denmark
[2] Department of Chemical Engineering, Universidad de Alcalá, 28805 Alcalá de Henares, Madrid, Spain
[3] Instituto de Catalisis y Petroleoquímica, ICP-CSIC, Marie Curie 2, 28049 Madrid, Spain.
[4] Research Center: Renewable Energy Systems and Recycling, Transilvania University of Brasov, Eroilor 29, 500036, Brasov, Romania

‡ Equally contributing authors

* Corresponding author: georgiana.amariei@bce.au.dk

Contents:

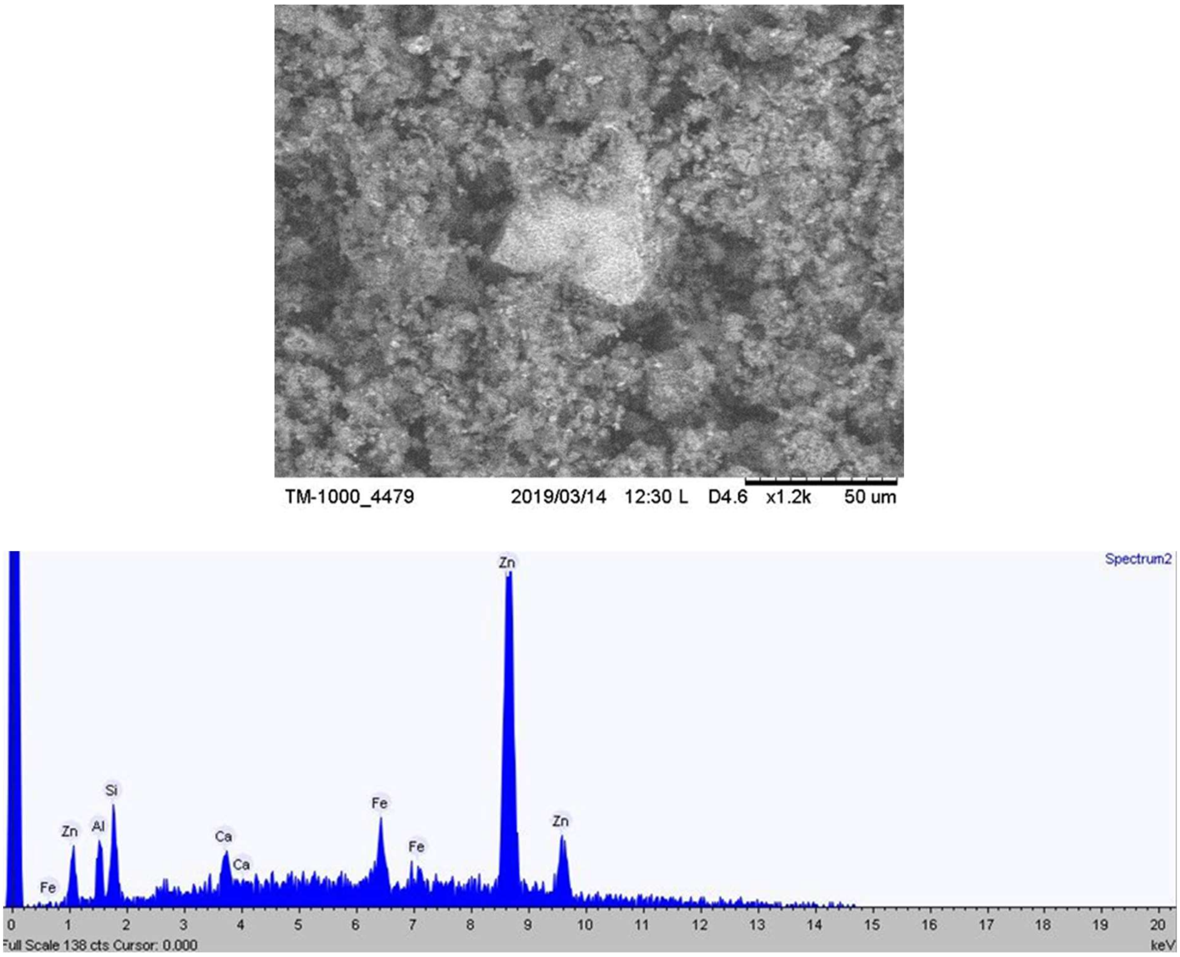

Figure S1. SEM image and EDX spectrum of ZnO-ZFA.

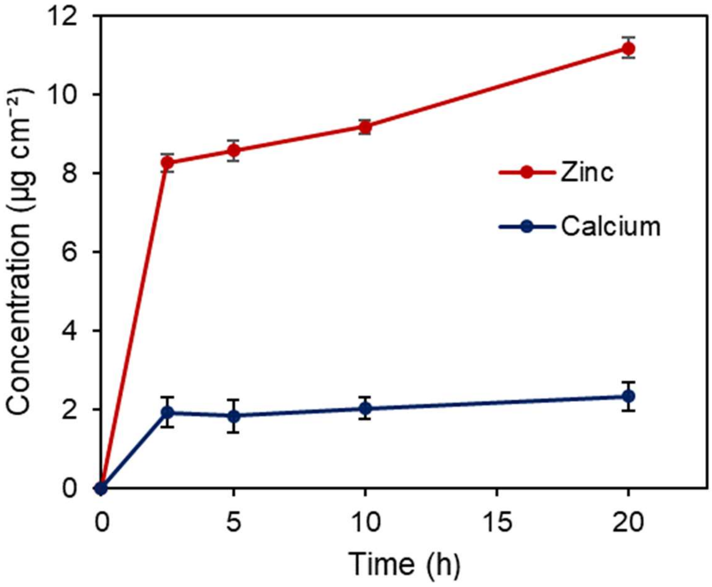

Figure S2. Solubilization of metal ions from ZnO-ZFA coatings at 37 ºC.

https://doi.org/10.1016/j.jece.2022.107603

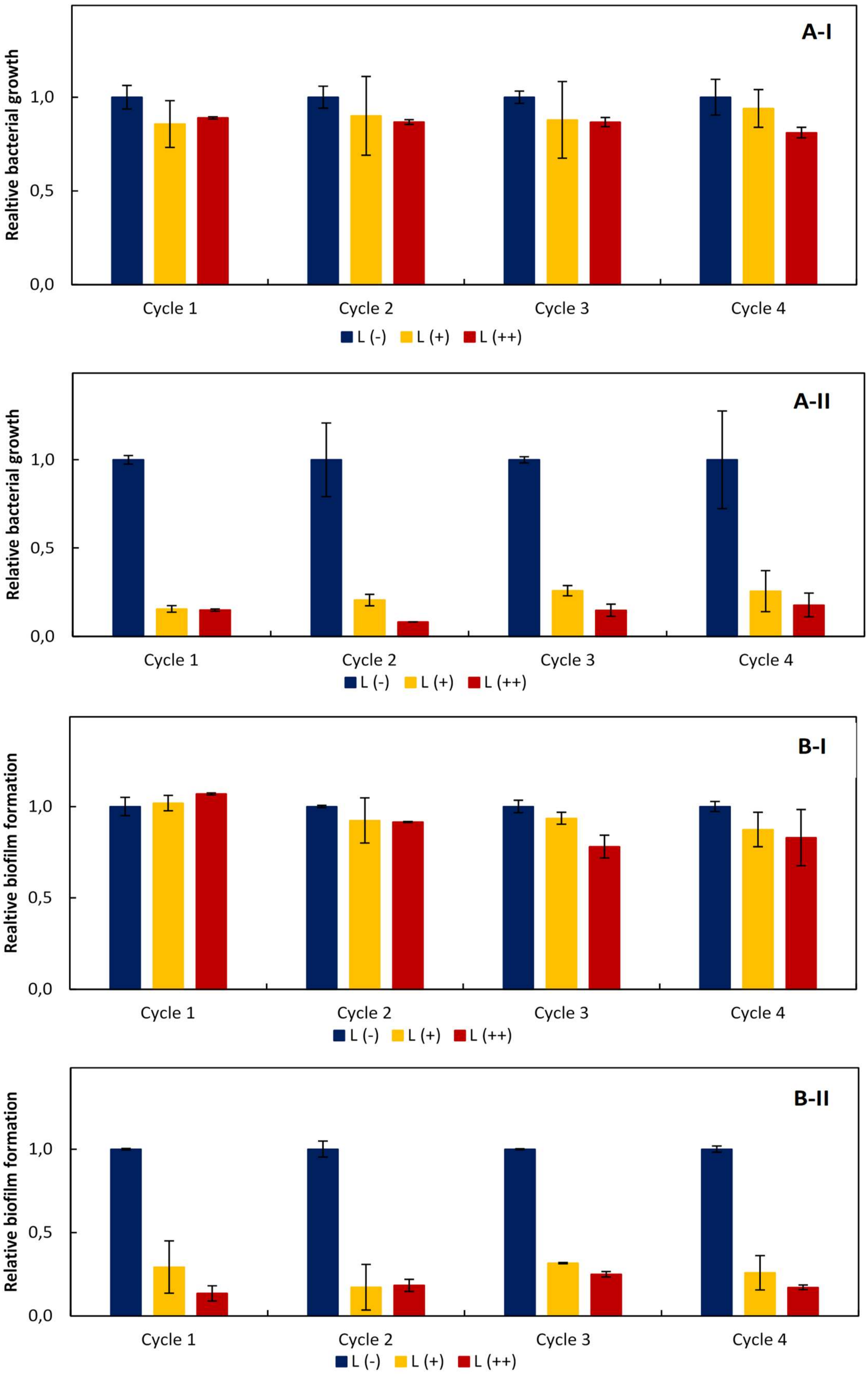

Figure S3. Reusability of un-coated (I) and ZnO-ZFA (II) coatings against *S. aureus* in liquid (A) and surface (B), under 365 nm UVA: L(-): without irradiation; L(+): 1.0 kW-h m^{-2} (winter-fall); and L(++): 2.0 kW-h m^{-2} (summer-spring).

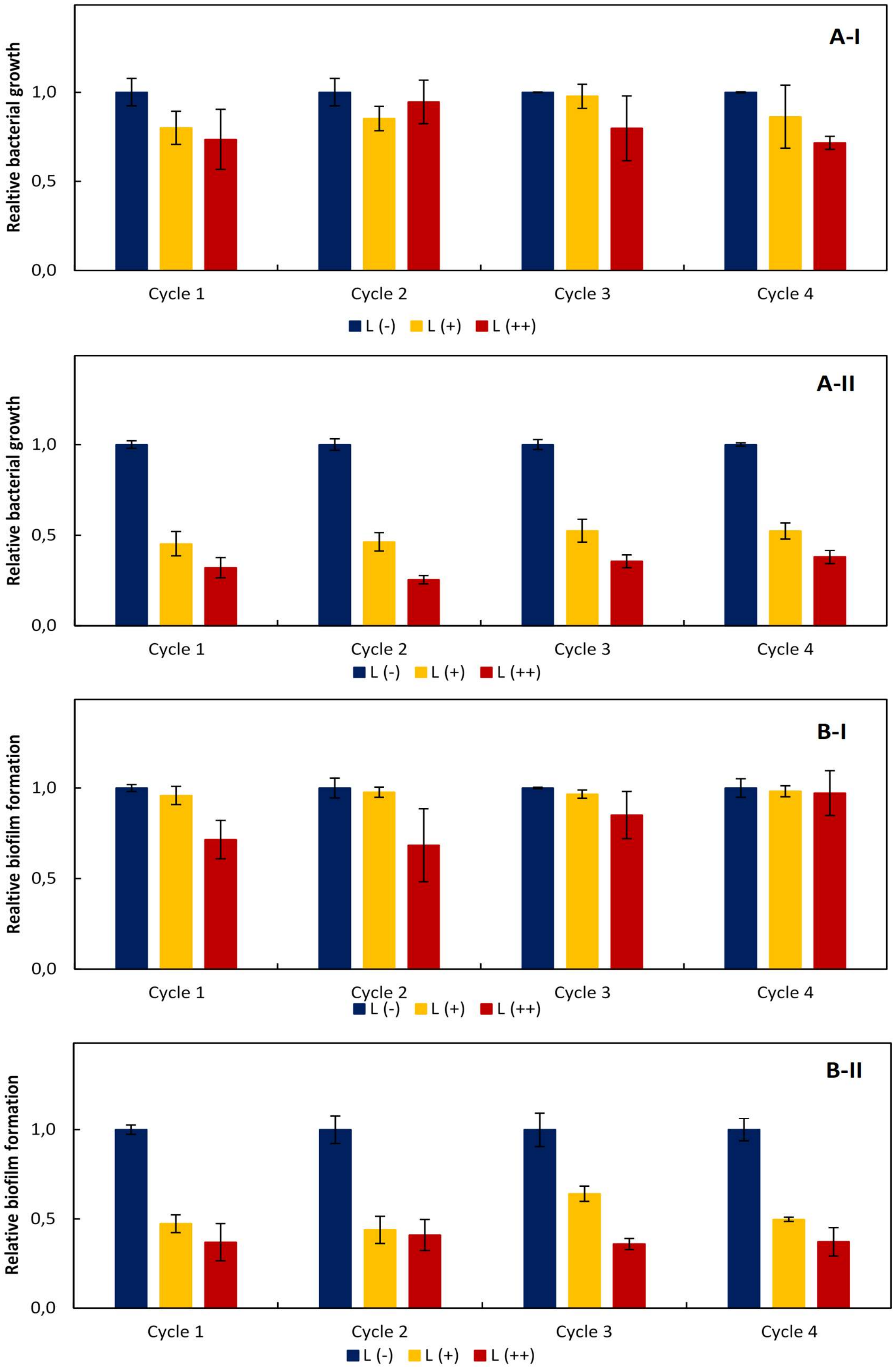

Figure 4. Reusability of un-coated (I) and ZnO-ZFA (II) coatings against *E. coli* in liquid (A) and surface (B), under 365 nm UVA: L(-): without irradiation; L(+): 1.0 kW-h m^{-2} (winter-fall); and L(++): 2.0 kW-h m^{-2} (summer-spring).

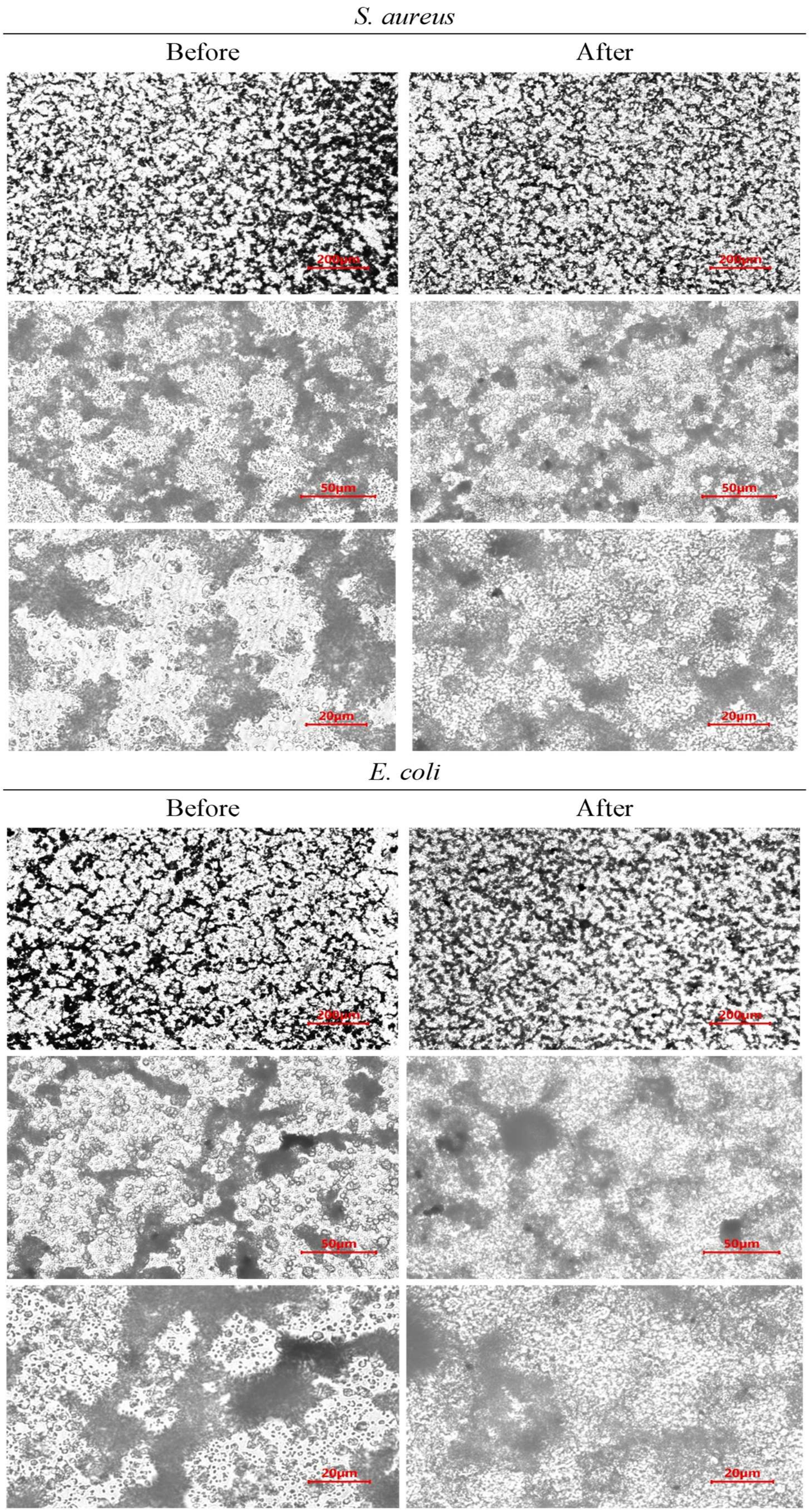

Figure S5. Optical microscope images of ZnO-ZFA coatings before and after 4 cycles of (photo)disinfection.

https://doi.org/10.1016/j.jece.2022.107603

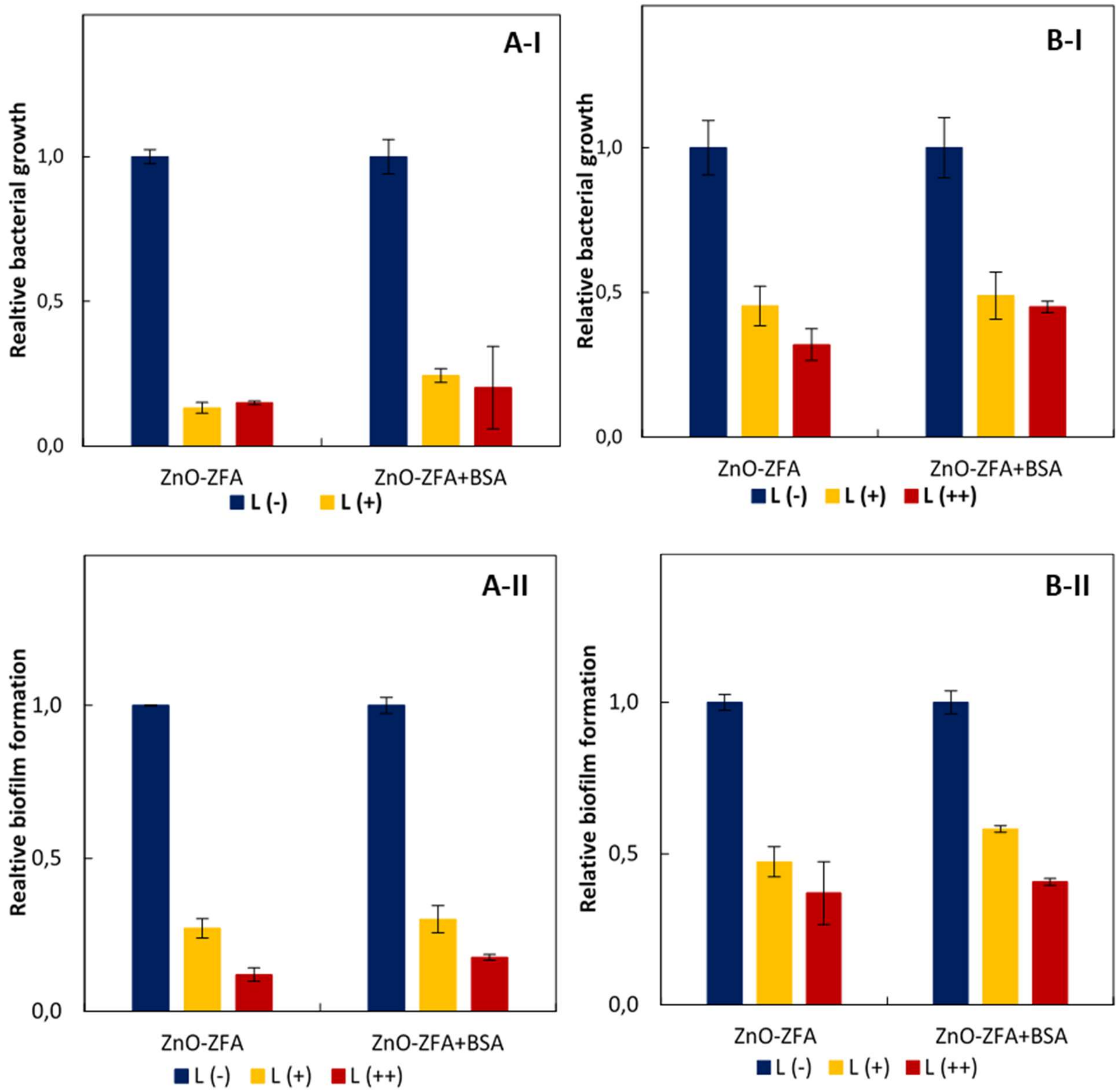

Figure S6. Bacterial (I) and biofilm (II) inhibition for clean ZnO-ZFA coatings and organic fouled ZnO-FA coatings (ZnO-ZFA+BSA) against *S. aureus* (A) and *E. coli* (B), under 365 nm UVA irradiation with coatings of ZnO-ZFA previously incubated in the dark for 20h: L(-): without irradiation; L(+): 1.0 kW-h m^{-2} (winter-fall); and L(++): 2.0 kW-h m^{-2} (summer-spring).

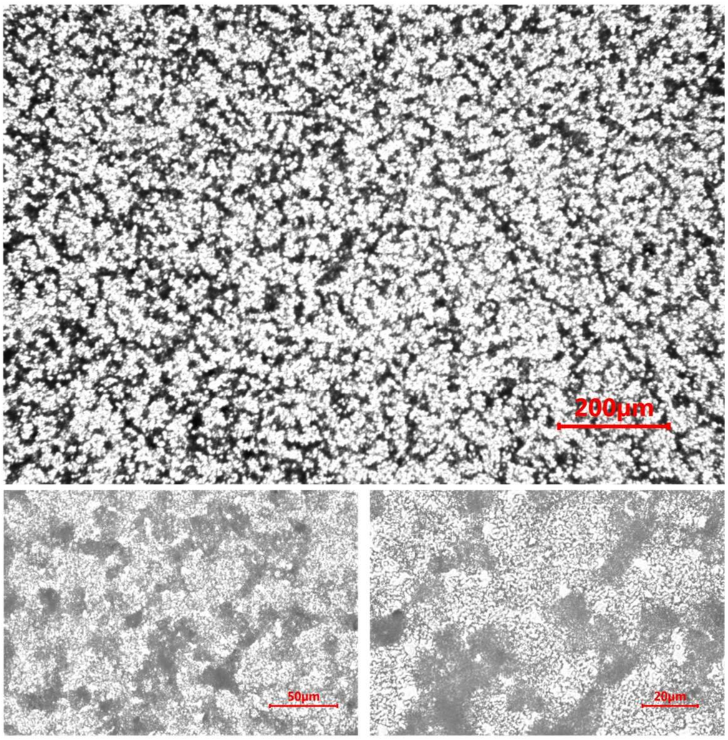

Figure S7. Optical microscope images of the ZnO-ZFA functionalized surfaces after overnight contact with BSA.

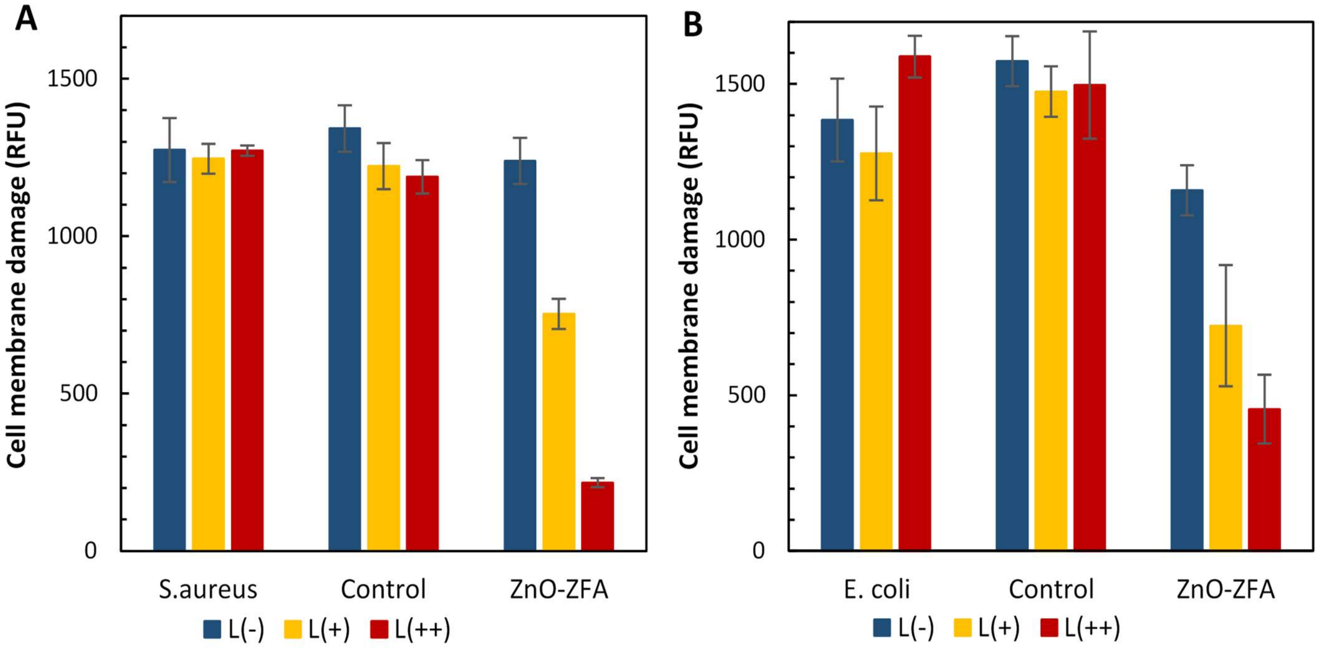

Figure S8. Cell membrane damage (Relative Units of Fluorescence, RFU) for *S. aureus* (A) and *E. coli* (A), under 365 nm UVA irradiation with coatings of ZnO-ZFA previously incubated in the dark for 20h: L(-): without irradiation; L(+): 1.0 kW-h m^{-2} (winter-fall); and L(++): 2.0 kW-h m^{-2} (summer-spring).

https://doi.org/10.1016/j.jece.2022.107603

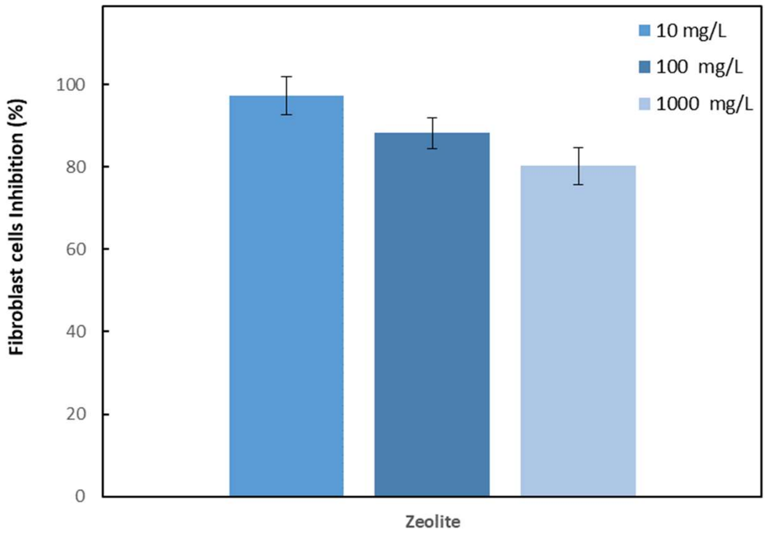

Figure S9. Cell viability of human dermal fibroblasts after 24 -hrs contact with different concentrations of ZnO-ZFA, as calculated from the MTT assay.

Table S1. Summary of the performance of the selected photocatalytic materials compared to ZnO-ZFA for the degradation of ciprofloxacin (CIP).

Experimental conditions						**Performance**	**Ref.**
pH	CIP (mg/L)	Catalyst		Irradiation source	Time (min)	Degradation (%)	
		Type	Conc. (g/L)				
-	10	$ZnO/AgVO_3$	0.1	UV-Vis	120	93.1	[1]
–	20	N-TiO_2	3	Vis (≥420 nm)	90	90	[2]
-	20	Fe–N–TiO_2	1	Vis	360	70	[3]
-	10	Fe-$BiVO_4$	1	UV-Vis	30	100	[4]
-	10	$CuS/BiVO_4$	1	Vis	90	83	[5]
–	10	CeO_2–Ag/AgBr	0.25	Vis (≥420 nm)	120	93.1	[6]
–	20	g-C_3N_4/Ti_3C_2	0.2	Vis (≥420 nm)	150	100	[7]
10	4	ZnO	0.02	UVA (365nm)	40	48	[8]
10	40	ZnO	1.2	UV-Vis	180	90	[9]
9	50	S,N-MgO	0.1	UVA (365nm)	30	99	[10]
7	4	ZnO	0.02	UVA (365nm)	40	42	[8]
7	10	rGO-ZnO-$BiVO_4$	0.3	Vis	60	98.4	[11]
7	10	BiOCl/diatomite	0.5	UV-Vis (320–780nm)	30	94	[12]
7	10	Ag@PCNS/$BiVO_4$	1	Vis (≥420 nm)	120	92,7	[13]
7	10	$Mn_2O_3/Mn_3O_4/MnO_2$	0.2	Vis (≥420 nm)	40	95.6	[14]
6.3	5	TiO_2/g-C_3N_4	0.2	UV-Vis	60	93.4	[15]
6	25	$BiOBr/TiO_2$	1	Vis (≥420 nm)	150	95.5	[16]
				UV-Vis	150	100	
5.5	50	N,S co-doped TiO_2	0.05	UV-Vis (320-780 nm)	150	78.7	[17]
5	3	TiO_2	1	UVC (≥254nm)	105	92.8	[18]
5	20	TiO_2/montmorillonite	0.1	UVA	120	45	[19]
				UVB		55	
				UVC		60	
4	4	ZnO	0.02	UVA (365nm)	40	18	[8]
4	10	ZnO-ZFA	0.5	UVA (365nm)	60	100	This study

https://doi.org/10.1016/j.jece.2022.107603

References

[1] S. Song, K. Wu, H. Wu, J. Guo, L. Zhang, Synthesis of Z-scheme multi-shelled ZnO/AgVO3 spheres as photocatalysts for the degradation of ciprofloxacin and reduction of chromium(VI). J. Mater. Sci. 55 (2020) 4987-5007. 10.1007/s10853-019-04316-8.

[2] X. Xing, Z. Du, J. Zhuang, D. Wang, Removal of ciprofloxacin from water by nitrogen doped TiO 2 immobilized on glass spheres: Rapid screening of degradation products. J. Photochem. Photobiol. A: Chem. 359 (2018) 23-32. 10.1016/j.jphotochem.2018.03.026.

[3] T. Suwannaruang, J. P. Hildebrand, D. H. Taffa, M. Wark, K. Kamonsuangkasem, P. Chirawatkul, K. Wantala, Visible light-induced degradation of antibiotic ciprofloxacin over Fe–N–TiO2 mesoporous photocatalyst with anatase/rutile/brookite nanocrystal mixture. J. Photochem. Photobiol. A: Chem. 391 (2020) 112371. 10.1016/j.jphotochem.2020.112371.

[4] D. B. Hernández-Uresti, C. Alanis-Moreno, D. Sanchez-Martinez, Novel and stable Fe-BiVO4 nanocatalyst by efficient dual process in the ciprofloxacin degradation. Mater. Sci. Semicond. Process. 102 (2019) 104585. 10.1016/j.mssp.2019.104585.

[5] C. Lai, M. Zhang, B. Li, D. Huang, G. Zeng, L. Qin, X. Liu, H. Yi, M. Cheng, L. Li, Z. Chen, L. Chen, Fabrication of CuS/BiVO4 (0 4 0) binary heterojunction photocatalysts with enhanced photocatalytic activity for Ciprofloxacin degradation and mechanism insight. Chem. Eng. J. 358 (2019) 891-902. 10.1016/j.cej.2018.10.072.

[6] X.-J. Wen, C.-G. Niu, L. Zhang, C. Liang, H. Guo, G.-M. Zeng, Photocatalytic degradation of ciprofloxacin by a novel Z-scheme CeO2–Ag/AgBr photocatalyst: Influencing factors, possible degradation pathways, and mechanism insight. J. Catal. 358 (2018) 141-154. 10.1016/j.jcat.2017.11.029.

[7] N. Liu, N. Lu, Y. Su, P. Wang, X. Quan, Fabrication of g-C3N4/Ti3C2 composite and its visible-light photocatalytic capability for ciprofloxacin degradation. Sep. Purif. Technol. 211 (2019) 782-789. 10.1016/j.seppur.2018.10.027.

[8] M. El-Kemary, H. El-Shamy, I. El-Mehasseb, Photocatalytic degradation of ciprofloxacin drug in water using ZnO nanoparticles. J. Lumin. 130 (2010) 2327-2331. 10.1016/j.jlumin.2010.07.013.

[9] J. Xiong, W. Li, K. Zhao, W. Li, G. Cheng, Engineered zinc oxide nanoaggregates for photocatalytic removal of ciprofloxacin with structure dependence. J Nanopart Res. 22 (2020) 10.1007/s11051-020-04881-z

[10] S. Akbari, G. Moussavi, S. Giannakis, Efficient photocatalytic degradation of ciprofloxacin under UVA-LED, using S,N-doped MgO nanoparticles: Synthesis, parametrization and mechanistic interpretation. J. Mol. Liq. 324 (2021) 11483. 10.1016/j.molliq.2020.114831.

[11] A. Raja, P. Rajasekaran, K. Selvakumar, M. Arunpandian, K. Kaviyarasu, S. Asath Bahadur, M. Swaminathan, Visible active reduced graphene oxide-BiVO4-ZnO ternary photocatalyst for efficient removal of ciprofloxacin. Sep. Purif. Technol. 233 (2020) 115996. 10.1016/j.seppur.2019.115996.

[12] Z. Jia, T. Li, Z. Zheng, J. Zhang, J. Liu, R. Li, Y. Wang, X. Zhang, Y. Wang, C. Fan, The BiOCl/diatomite composites for rapid photocatalytic degradation of ciprofloxacin: Efficiency, toxicity evaluation, mechanisms and pathways. Chemical Engineering Journal 380 (2020) 122422. 10.1016/j.cej.2019.122422.

[13] Y. Deng, L. Tang, C. Feng, G. Zeng, J. Wang, Y. Zhou, Y. Liu, B. Peng, H. Feng, Construction of plasmonic Ag modified phosphorous-doped ultrathin g-C3N4 nanosheets/BiVO4 photocatalyst with enhanced visible-near-infrared response ability for ciprofloxacin degradation. Journal of hazardous materials 344 (2018) 758-769. 10.1016/j.jhazmat.2017.11.027.

[14] J. Zhao, Z. Zhao, N. Li, J. Nan, R. Yu, J. Du, Visible-light-driven photocatalytic degradation of ciprofloxacin by a ternary Mn2O3/Mn3O4/MnO2 valence state heterojunction. Chem. Eng. J. 353 (2018) 805-813. 10.1016/j.cej.2018.07.163.

[15] K. Hu, R. Li, C. Ye, A. Wang, W. Wei, D. Hu, R. Qiu, K. Yan, Facile synthesis of Z-scheme composite of TiO2 nanorod/g-C3N4 nanosheet efficient for photocatalytic degradation of ciprofloxacin. J. Clean. Prod. 253 (2020) 120055. 10.1016/j.jclepro.2020.120055.

[16] J. Rashid, A. Abbas, L. C. Chang, A. Iqbal, I. U. Haq, A. Rehman, S. U. Awan, M. Arshad, M. Rafique, M. A. Barakat, Butterfly cluster like lamellar BiOBr/TiO2 nanocomposite for enhanced sunlight photocatalytic mineralization of aqueous ciprofloxacin. Sci. Total Environ. 665 (2019) 668-677. 10.1016/j.scitotenv.2019.02.145.

[17] L. T. Nguyen, H. T. Nguyen, T.-D. Pham, T. D. Tran, H. T. Chu, H. T. Dang, V.-H. Nguyen, K. M. Nguyen, T. T. Pham, B. Van der Bruggen, UV–Visible Light Driven Photocatalytic Degradation of Ciprofloxacin by N,S Co-doped TiO2: The Effect of Operational Parameters. Top. Catal. 63 (2020) 985-995. 10.1007/s11244-020-01319-7.

[18] M. Malakootian, A. Nasiri, M. Amiri Gharaghani, Photocatalytic degradation of ciprofloxacin antibiotic by TiO2 nanoparticles immobilized on a glass plate. Chem. Eng. Commun. 207 (2019) 56-72. 10.1080/00986445.2019.1573168.

[19] A. Hassani, A. Khataee, S. Karaca, Photocatalytic degradation of ciprofloxacin by synthesized TiO2 nanoparticles on montmorillonite: Effect of operation parameters and artificial neural network modeling. J. Mol. Catal. A Chem. 409 (2015) 149-161. 10.1016/j.molcata.2015.08.020.